Physical Chemistry Chemical Physics
Electronic Supplementary Information

Pulsed electron spin nutation spectroscopy of weakly exchange-coupled biradicals: A general theoretical approach and determination of the spin dipolar interaction

Kazuki Ayabe,[†,‖] Kazunobu Sato,[†,‖,*] Shinsuke Nishida,[†,‖] Tomoaki Ise,[†,‖] Kenji Sugisaki,[†,‖] Shigeaki Nakazawa,[†,‖] Yasushi Morita,[‡,‖,*] Kazuo Toyota,[†,‖] Daisuke Shiomi,[†,‖] Masahiro Kitagawa,[§,‖] and Takeji Takui,[†,‖,*]

[†]Department of Chemistry and Molecular Materials Science,
Graduate School of Science, Osaka City University,
3-3-138 Sugimoto, Sumiyoshi-ku, Osaka 558-8585, Japan,
[‡]Department of Chemistry, Graduate School of Science, Osaka University,
1-1 Machikaneyama, Toyonaka, Osaka 560-0043, Japan,
[§]Department of System Innovation, Graduate School of Engineering Science, Osaka University,
1-3 Machikaneyama, Toyonaka, Osaka 560-8531, Japan,
[‖]Japan Science and Technology Agency (JST), Sanban-cho, Chiyoda-ku, Tokyo 102-0075, Japan

Contents

References

1. Synthesis and chemical identification of biradical 1

Synthesis

General: Melting points were measured with a hot-stage apparatus and are uncorrected. R_f values on TLC were recorded on E. Merck precoated (0.25 mm) silica gel 60 F_{254} plates. The plates were sprayed with a solution of 10% phosphomolybdic acid in 95% ethanol and then heated until the spots became clearly visible. High resolution-MS (ESI) spectra and elemental analyses were performed at the Graduate School of Science, Osaka City University. Silica gel 60 (100—200 mesh) deactivated by mixing with 6% water was used for column chromatography. CH_2Cl_2 and *N,N*-dimethylformamide (DMF) as solvents were dried over CaH_2 and distilled under argon prior to use. OXONE ($2KHSO_5 \cdot KHSO_4 \cdot K_2SO_4$) was purchased from Aldrich. 4-Hydroxy-2,2,6,6-tetra[($^2H_3$)methyl]-[3,3-$^2H_2$,4-$^2H_1$,5,5-$^2H_2$]piperidin-*N*-oxyl (TEMPOL-d_{17}) (98 atom% D) and 4-hydroxy-2,2,6,6-tetra[($^2H_3$)methyl]-[3,3-$^2H_2$,4-$^2H_1$,5,5-$^2H_2$,^{15}N]piperidin-^{15}*N*-oxyl (TEMPOL-^{15}*N*-d_{17}) (98 atom% D; 99 atom% ^{15}N) were purchased from CDN Isotopes. All the purchased reagents were used for reaction without further purification. An isotope-labelled biradical **1** is classified as a new compound and the synthetic route is given in Scheme S1 as follows:

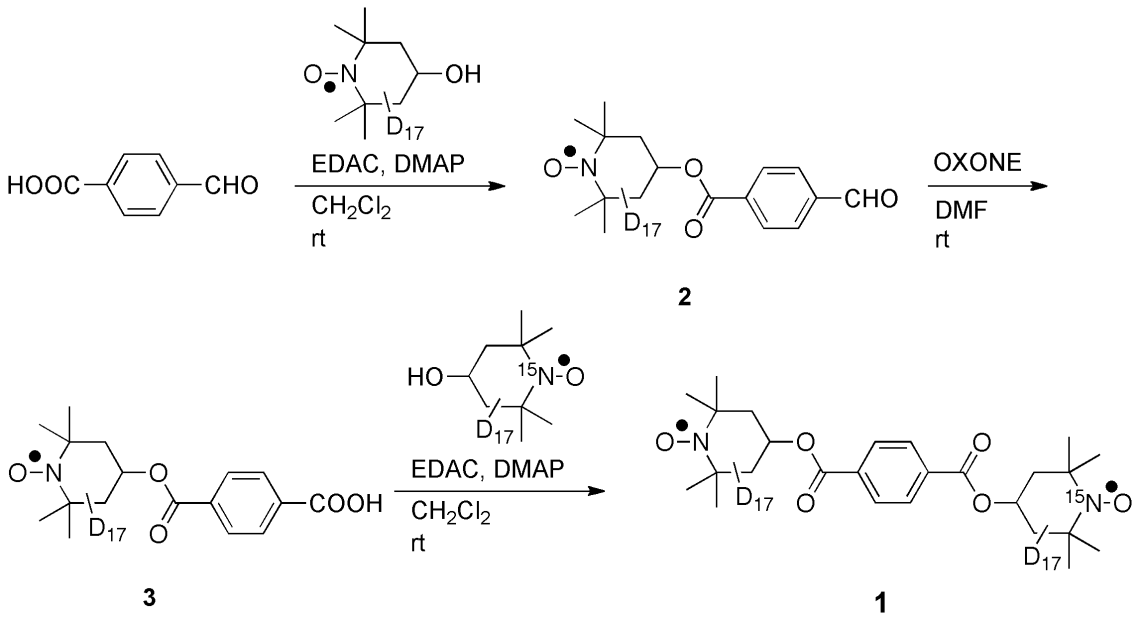

Scheme S1

2,2,6,6-Tetra[($^2H_3$)methyl]-[3,3-$^2H_2$,4-$^2H_1$,5,5-$^2H_2$]piperidin-*N*-oxyl-4-yl 4-formylbenzoate (2) TEMPOL-d_{17} (100 mg, 0.53 mmol), 4-formylbenzoic acid (158 mg, 1.06 mmol), *N*-ethyl-*N'*-dimethylaminopropylcarbodiimide hydrochloride (EDAC) (203 mg, 1.06 mmol), and 4-dimethylaminopyridine (DMAP) (130 mg, 1.06 mmol) were placed in a 20-mL Schlenk-tube. The mixture was dissolved with CH_2Cl_2 (1.5 mL) and stirred at room temperature under argon atmosphere for 20 h. After evaporation of the solvent, the residue was subjected to silica gel column chromatography with 10:1~4:1 mixture of hexane and ethyl acetate as eluent, to give **2** (95 mg, 56%) as an orange powder. mp. 130–132 °C; TLC R_f 0.6 (1:1 hexane/ethyl acetate); HRMS (ESI) Calcd for $C_{17}H_5D_{17}NO_4Na$ $[M + Na]^+$, 344.2514; Found,

344.2474; Anal. Calcd for $C_{17}H_5D_{17}NO_4$: C, 63.25; H, 1.57; D, 10.65; N, 4.36. Found: C, 63.32; H, 1.55; D, 10.54; N, 4.36.

4-(2,2,6,6-Tetra[($^2H_3$)methyl]-[3,3-$^2H_2$,4-$^2H_1$,5,5-$^2H_2$]piperidin-*N*-oxyl-4-oxycarbonyl)benzoic acid (3). The aldehyde derivative **2** (50 mg, 0.16 mmol) was placed in a 10-mL round-bottomed flask and dissolved with DMF (1.5 mL). To the mixture was added OXONE (98 mg, 0.16 mmol) and stirred at room temperature for 2.5 h. OXONE (98 mg, 0.16 mmol) was added and stirred at 1.5 h. The reaction mixture was washed with satd NaCl aqueous solution and extracted with ethyl acetate. The organic extracts were combined and dried over Na_2SO_4, then filtered and concentrated under reduced pressure, to give a carboxylic acid derivative **3** (40 mg, 75%) as an orange powder. This compound was used for the next reaction without purification. mp. 171–173 °C; TLC R_f 0.2 (1:1 hexane/ethyl acetate); HRMS (ESI) Calcd for $C_{17}H_5D_{17}NO_5Na$ $[M + Na]^+$, 360.2463; Found, 360.2472.

(2,2,6,6-Tetra[($^2H_3$)methyl]-[3,3-$^2H_2$,4-$^2H_1$,5,5-$^2H_2$]piperidin-*N*-oxyl-4-yl) (2,2,6,6-tetra[($^2H_3$)methyl]-[3,3-$^2H_2$,4-$^2H_1$,5,5-$^2H_2$,^{15}N]piperidin-^{15}*N*-oxyl-4-yl) terephthalate (1). The acid derivative **3** (20 mg, 0.06 mmol), TEMPOL-^{15}N-d_{17} (11 mg, 0.06 mmol), EDAC (12 mg, 0.06 mmol), and DMAP (7 mg, 0.06 mmol) were placed in a 20-mL Schlenk-tube and dissolved with CH_2Cl_2 (1.5 mL). The mixture was stirred at room temperature under argon atmosphere for 20 h. After evaporation of the solvent, the residue was subjected to silica gel column chromatography with 10:1~4:1 mixture of hexane and ethyl acetate as eluent, to give the biradical **1** (18 mg, 59%) as an orange powder. mp 214–216 °C; TLC R_f 0.5 (1:1 hexane/ethyl acetate); HRMS (ESI) Calcd for $C_{26}H_4D_{34}O_6N\,^{15}NNa$ $[M + Na]^+$, 532.4732; Found, 532.4716; Anal. Calcd for $C_{26}H_4D_{34}O_6N^{15}N(CH_2Cl_2)_{0.4}$: C, 58.31; H, 0.89; D, 12.59; N, 5.33. Found: C, 58.41; H, 0.75; D, 12.77; N, 5.20.

2. Pulse sequences of X-band 2D-ESN (or ESTN) and Q-band 3-pulse/4-pulse ELDOR spectroscopy

Figure S1 shows the pulse sequences used in pulsed electron spin magnetic resonance spectroscopy in this work, i.e. pulse-based X-band 2D Electron Spin Transient Nutation (ESN or ESTN) and pulse-based Q-band ELectron–electron DOuble Resonance (ELDOR) spectroscopy for non-oriented media. In the 2D-ESN experiments, two schemes of the pulse sequences, (a) electron-spin-echo detected and (b) FID-detected, were used. The FID-detected sequence was applied to a single crystal of DPPH which does not generate the spin echo signal. In order to completely maintain the same experimental conditions for both the target molecule and the external reference for the microwave irradiation strength at the particular microwave frequency, both the chemical entities were positioned in a single sample tube. We have set a particular interval time between the pulses in the sequence (a) to be 400 ns. This time setting can afford to completely differentiate between the nutation phenomena arising from biradical **1** and DPPH under the same experimental conditions except the detection scheme.

In the Q-band pulsed ELDOR spectroscopy, we have used the pulse sequence given in (c). In recent years, pulsed ELDOR experiments are carried out with a dead-time free 4-pulse sequence as given in (d). We have also applied the 4-pulse sequence to detect the ELDOR signal of biradical **1**, which can afford to give a more distinct oscillation at the shorter time of t_3. The DeerAnalysis of our ELDOR signal has given the main component of the distance between the two spins at the nitroxide sites to be 1.64 nm.

The experimental parameters used for the pulse experiments are as follows. The echo-detected 2D-ESTN; (a) ν_{MW} = 9.651658 GHz, the separation times of pulses are t_1 = (40 + 8×n_1) ns, t_2 = 400 ns, and the duration time of pulses are P_0 = (8 + 8×n_1) ns, P_1 = 16 ns and P_2 = 32 ns (n_1 = 0, 1, …, 63). The FID-detected 2D-ESTN; (b) ν_{MW} = 9.651733 GHz, t_p = 8 ns and Δt_p = (8×n_1) ns (n_1 = 0, 1, …, 63). The 3-pulse ELDOR; (c) P_0 = P_1 = 30 ns, P_2 = 40 ns, t_1 = 1200 ns, t_2 = (4×n_2) ns (n_2 = 0, 1, …, 256), ν_A = 33.813352 GHz and ν_B = 33.878352 GHz.

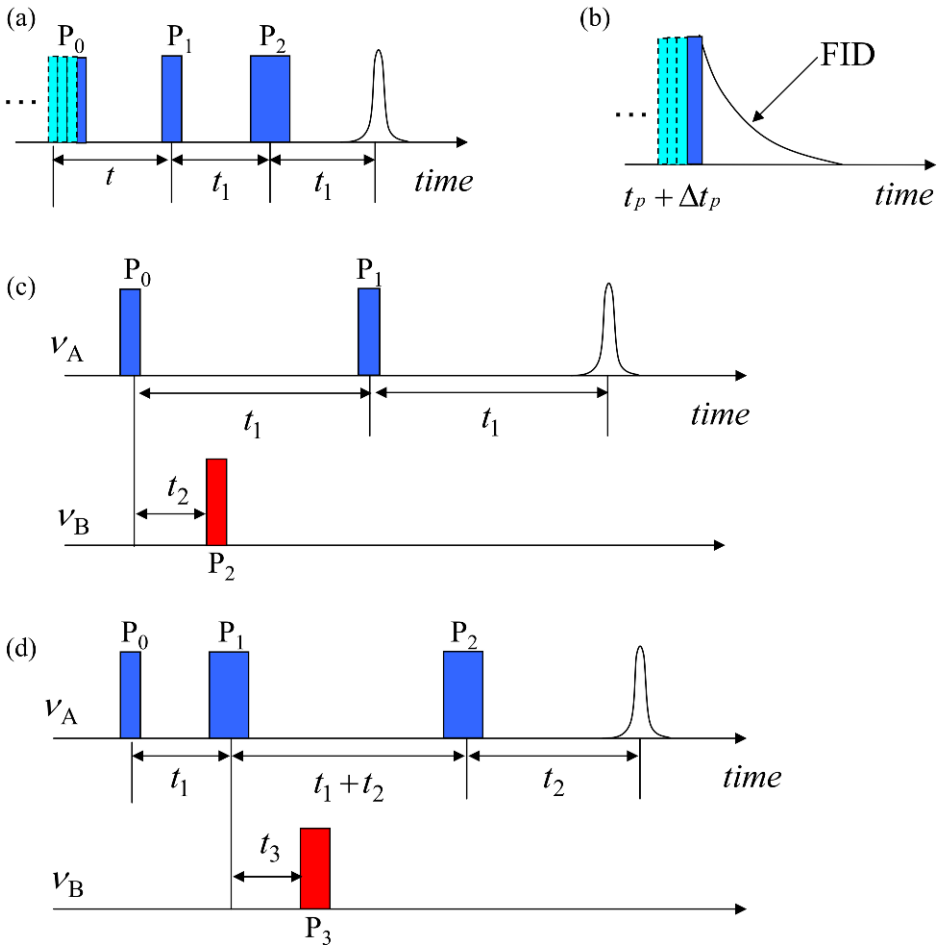

Figure S1 (a)–(d). Pulse sequences for the 2D-ESTN and 3-pulse/4-pulse ELDOR experiments. (a) Pulse sequence for the echo-detected 2D-ESTN measurements. (b) Pulse sequence for the FID-detected 2D-ESTN measurements. (c) Pulse sequence for the 3-pulse ELDOR experiments: The microwave pulse with the pulse length P_2 of the frequency ν_B is given in red. (d) Pulse sequence for the 4-pulse ELDOR experiments. The microwave pulse with the pulse length P_3 of the frequency ν_B is given in red.

3. CW ESR spectra of biradical 1 observed in a toluene solution

Figure S2 shows the CW X-band ESR spectra (in blue) of biradical **1** observed in a toluene solution at room temperature and the simulated ones (in red) (ν_{MW} = 9.746698 GHz, T = 296 K). The spectral simulation for the spin-Hamiltonian parameters was carried out by using the EasySpin programme package [S1]. It should be noted that for the exchange coupling J_{12} value over 0.7 MHz absorption peaks artificially split on the 'pepper' command in the programme. In order to avoid this artefact, we have made the spectral simulation for the two radicals (^{14}N-TEMPO and ^{15}N-TEMPO) independently existing in solution using the 'garlic' command. The line shape analysis contains the anisotropic parameters of the spin-Hamiltonian.

From the simulation, we have determined the following parameters of biradical **1**: the anisotropic g-values of both the radical sites are g_{XX} = 2.0021, g_{YY} = 2.0061. g_{ZZ} = 2.0101. The hyperfine coupling parameters of the ^{14}N nucleus are $|A_{XX}(^{14}\mathrm{N})|$ = 96 MHz, $|A_{YY}(^{14}\mathrm{N})|$ = 17.72 MHz and $|A_{ZZ}(^{14}\mathrm{N})|$ = 16 MHz. Those of the ^{15}N nucleus are $|A_{XX}(^{15}\mathrm{N})|$ = 134.67 MHz, $|A_{YY}(^{15}\mathrm{N})|$ = 27.42 MHz and $|A_{ZZ}(^{15}\mathrm{N})|$ = 22.44 MHz. The definitions of the principal axes for the magnetic tensors are given in Figure 3 in the text. The rotation correlation time is t_c = 4.0×10^{-11} sec. The Lorentzian line shape having 0.049 mT of the full width at half maximum (FWHM) was assumed. Thus, $|A_{iso}(^{14}\mathrm{N})|$ = 43.24 MHz and $|A_{iso}(^{15}\mathrm{N})|$ = 60.63 MHz. are determined. The narrow line width is due to the deuteration of the methyl groups. Owing to the deuteration effect, satellite signals attributable to the ^{13}C nuclei with the natural abundance show up as seen in Figure S2. These peaks are satisfactorily reproduced by considering the natural abundance of ^{13}C (1.07 %) and $|A_{iso,1}(^{13}\mathrm{C})|$ = 10.5 MHz and $|A_{iso,2}(^{13}\mathrm{C})|$ = 17.5 MHz. The result of the DFT calculation, given in Table S1, suggests that $|A_{iso,1}(^{13}\mathrm{C})|$ is assignable to the carbon atom adjacent to the nitrogen nucleus of the piperidine ring, and $|A_{iso,2}(^{13}\mathrm{C})|$ to the one of the axial methyl group of the TEMPO moieties.

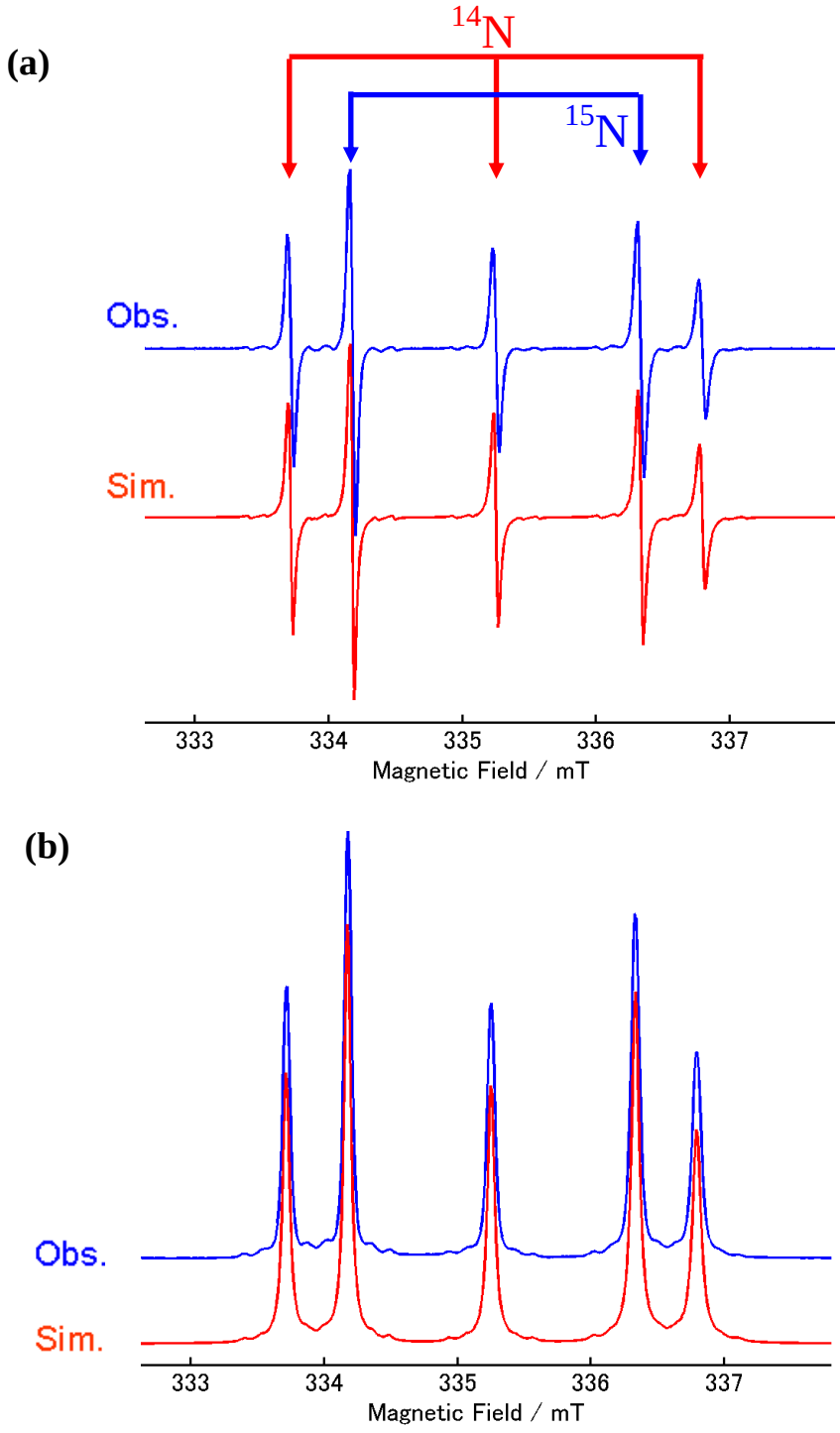

Figure S2. Observed and simulated CW ESR spectra of biradical **1** in a toluene solution (T = 296 K, ν_{MW} = 9.746698 GHz). The blue and red lines denote the observed and simulated spectra, respectively. (a) Upper: The observed and simulated spectra in the field-derivative mode and (b) bottom: The integrated spectra of those in (a).

Table S1. Calculated spin densities and isotropic hyperfine coupling constants (hfcc) of biradical **2**. The optimised molecular structure was obtained by the DFT calculation at the level of UB3LYP/6-31G(d). (a) N nuclei, (b) ^{13}C nuclei at the 2- or 6- positions of the piperidine ring, (c) ^{13}C nucleus at the axial methyl groups of the TEMPO moieties and (d) ^{13}C nucleus at the equatorial methyl of the TEMPO moieties. The numbering of the "atom" column of the table is based on the result of the DFT calculation of the isotope unlabeled biradical **2**, while the numbering of the "Position" column of the table is based on the IUPAC nomenclature.

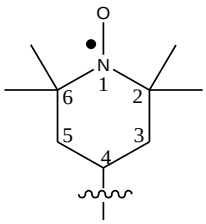

(a)

atom	Spin density	hfcc/MHz	Position
1N(^{14}N)	0.439236	39.46628	1 (piperidine)
22N(^{14}N)	0.439614	39.24592	1' (piperidine)

(b)

atom	Spin density	hfcc/MHz	Position
2C(^{13}C)	−0.017777	−7.67854	2 (piperidine)
6C(^{13}C)	−0.017893	−7.74440	6 (piperidine)
21C(^{13}C)	−0.018021	−7.96072	2' (piperidine)
23C(^{13}C)	−0.017927	−7.85036	6' (piperidine)

(c)

atom	Spin density	hfcc/MHz	Position
28C(^{13}C)	0.029336	15.61556	6-axial methyl
29C(^{13}C)	0.029428	15.80692	2-axial methyl
32C(^{13}C)	0.029390	15.82902	6'-axial methyl
34C(^{13}C)	0.029399	15.56494	2'-axial methyl

(d)

atom	Spin density	hfcc/MHz	Position
27C(^{13}C)	0.008573	8.33534	6-equatorial methyl
30C(^{13}C)	0.008556	8.36000	2-equatorial methyl
31C(^{13}C)	0.008714	8.45610	6'-equatorial methyl
33C(^{13}C)	0.008846	8.53312	2'-equatorial methyl

4. Discussion about any possibility of transesterification of biradical 1

Reference S2 showed that the ester bond is easy to be cleaved and transesterified as compared with the amide bond. There might be any possibility of biradical systems which have the same isotope labelled TEMPO moieties. In order to check any possibility of the transesterification, the spectral simulation of Q-band CW ESR spectra of biradical **1** from random orientation was carried out by assuming the existence of biradicals which have the same isotope labelled TEMPO sites. The results are shown in Figure S3. Comparing (a) and (b), as seen in the simulated spectrum, biradical **1** gives a prominent signal denoted by (i). On the other side, the intensity of the signal (ii) in the spectrum (b) becomes more stronger than in the spectrum (a). With decreasing the ratio of the transesterified biradicals, the simulated spectrum (b) approaches that in (a). As a result, we have concluded that there is less possibility of the transesterification of biradical **1**.

In the spectral simulation of biradical **1** in non-oriented media, we have set "Hstrain" parameters in the EasySpin programme to be 8 MHz for the *X*-, *Y*- and *Z*-directions of the molecular principal axes. Also, "Linewidth" is set to be 0.28 mT. Any physical reasons for the difference are not obvious in the present analysis.

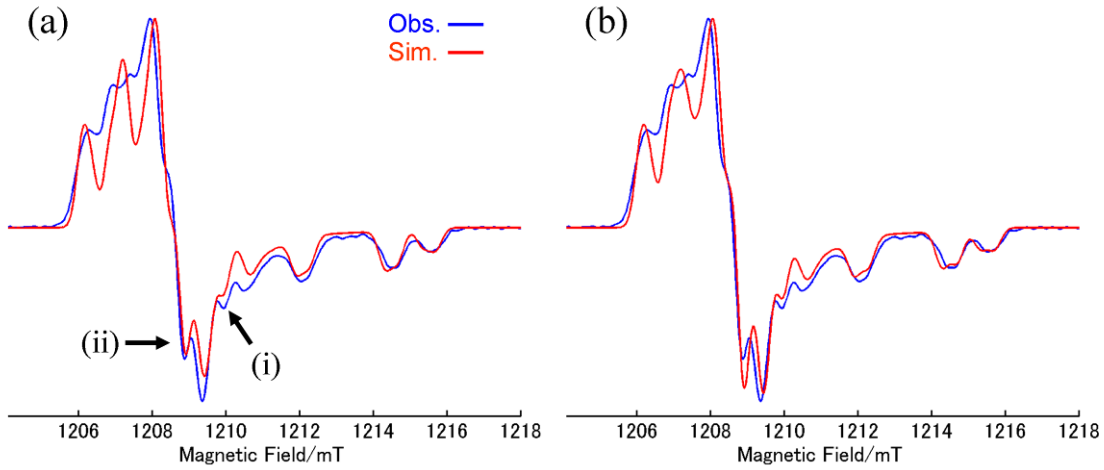

Figure S3. (a) Observed (blue line) and simulation (red line) spectra of biradical **1** in the frozen toluene glass. (b) The red line denotes the simulated spectrum which contains not only the signal of biradical **1** but also that of biradical with the same isotope labelled TEMPO moieties generated by the transesterification. The ratio of biradical spices is 1:1:1 (T = 50 K, ν_{MW} = 33.9653 GHz).

5. Effects of the J_{12} value of biradical 1 on the simulation of the random-orientation X-band CW spectrum

In reference S3, it has been reported that for biradicals with the spin-spin distance over 1.0 nm, the exchange interaction term J_{12} can be negligible in the spectral simulation. The magnitude of the term J_{12}, however, is influential in the line shapes of the spectra from random orientation, as illustrated in Figure S4. In biradical **1**, the line shape near 338 mT (signal appearing in the highest resonance field) in the X-band simulated spectra is influenced, as illustrated in Figure S5. Figure S5 shows that the line width at 338 mT becomes broader with increasing the J_{12} value. The influence is not remarkable, but an elaborate spectral simulation gives probable estimation of the J_{12} value with "sizable" spin dipolar interactions for biradicals with the spin distance less than 2.0 nm.

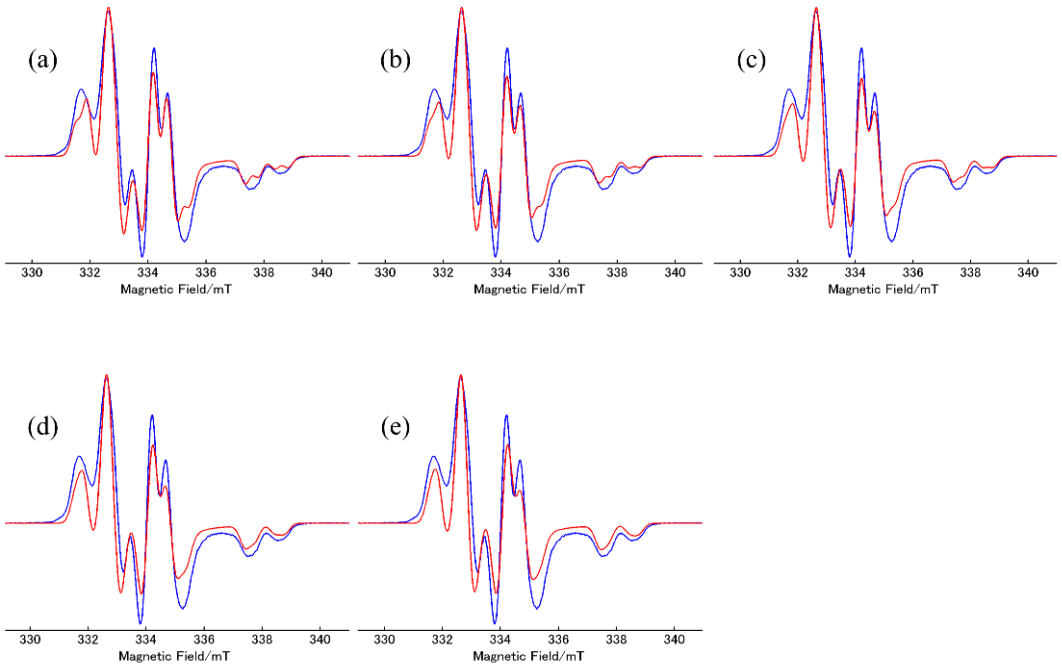

Figure S4. J_{12}-influence in the X-band spectral simulation of biradical **1**. The blue and red lines denote the observed and simulated spectra at 95 K, respectively. (a) J_{12} = 2 MHz. (b) J_{12} = 1 MHz. (c) J_{12} = 0 MHz. (d) J_{12} = −1 MHz. (e) J_{12} = −2 MHz.

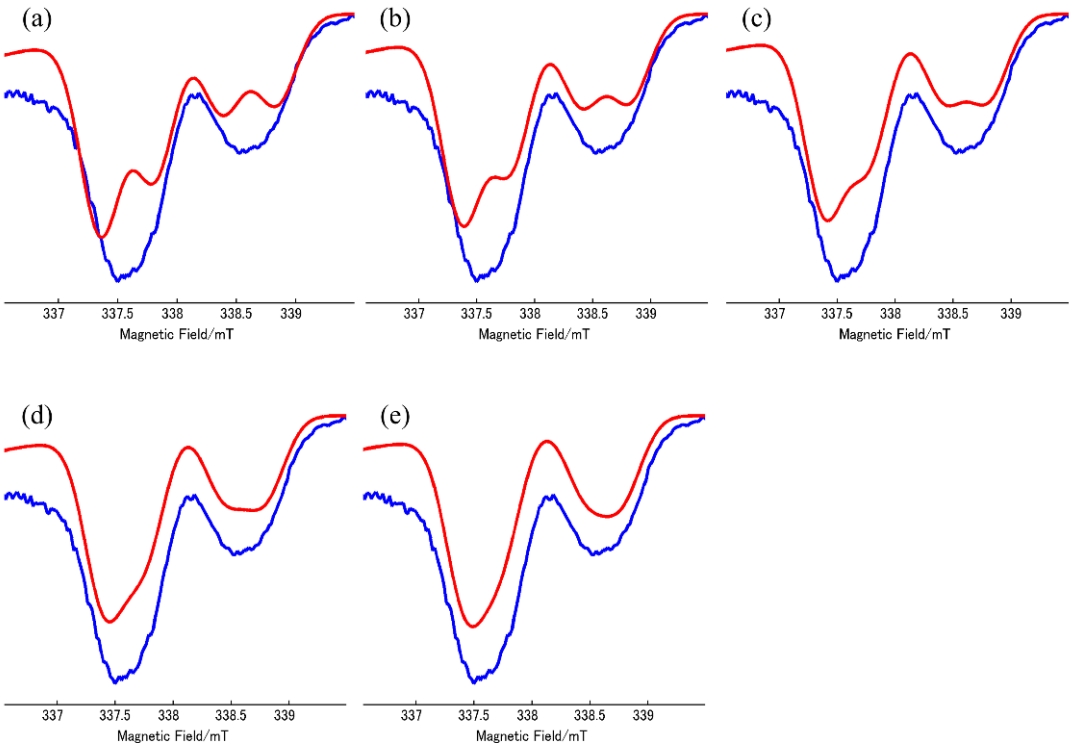

Figure S5. Close-up spectra of the peak near 339 mT in Figure S4. The blue and red lines denote the observed and simulated spectra at 95 K, respectively. (a) J_{12} = 2 MHz. (b) J_{12} = 1 MHz. (c) J_{12} = 0 MHz. (d) J_{12} = −1 MHz. (e) J_{12} = −2 MHz.

6. Details of the analysis of the nutation frequencies observed at the *X*-(or *Y*-) canonical orientation of biradical 1

Figure S6 shows the simulated spectra (in red) of the X-band echo detected field-swept ESR spectrum with respect to the canonical orientation. The signals from all the canonical orientations contribute to the signal near 344 mT, where we have observed the nutation frequency ω_n as a function of the microwave irradiated strength ω_1. In analysing the nutation phenomena at 344 mT, we have focused on the contributions from the *X*- and *Y*-canonical orientations, although we have noted that the contribution from the *Z*-orientation is less and shows up in the high-frequency range of the main nutation peak ($\omega_n/2\pi$ = 22.6 MHz). The approach above can be justified as follows:

(i) The behaviour of ω_n of the *Z*-orientation corresponding to the principal axis with the maximum value of the D_{12} tensor shows a smaller curvature in blue than that of the *X*- or *Y*-orientation, as given in Figure S7(b). This is due to the fact that the nutation frequency of the *Z*-orientation is higher than those of the other two orientations.

(ii) The parameter of the spin dipolar interaction $E_{12} = (D_{12,XX}-D_{12,YY})/2$ is vanishing for biradical **1**, leading to the axially symmetric D_{12} tensor. Thus, the number of the orientations which contribute to the nutation signal from the axial components is much greater than the *Z*-orientation.

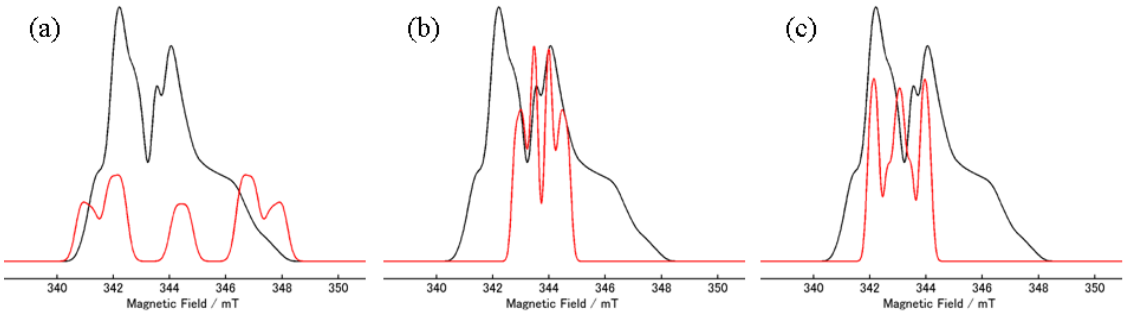

Figure S6. Simulated spectra of the echo-detected field-swept ESR spectrum at the X-band microwave frequency (ν_{MW} = 9.651697 GHz). The black line denotes the whole spectrum of biradical **1** from random orientation. The spectra in red in (a), (b) and (c) denote the simulated spectrum of the *X*-orientation, that of the *Y*-orientation and that of the *Z*-orientation. The spectral assignments are based on the definitions of the principal axes of the magnetic tensors, as given in Figure 3 in the text.

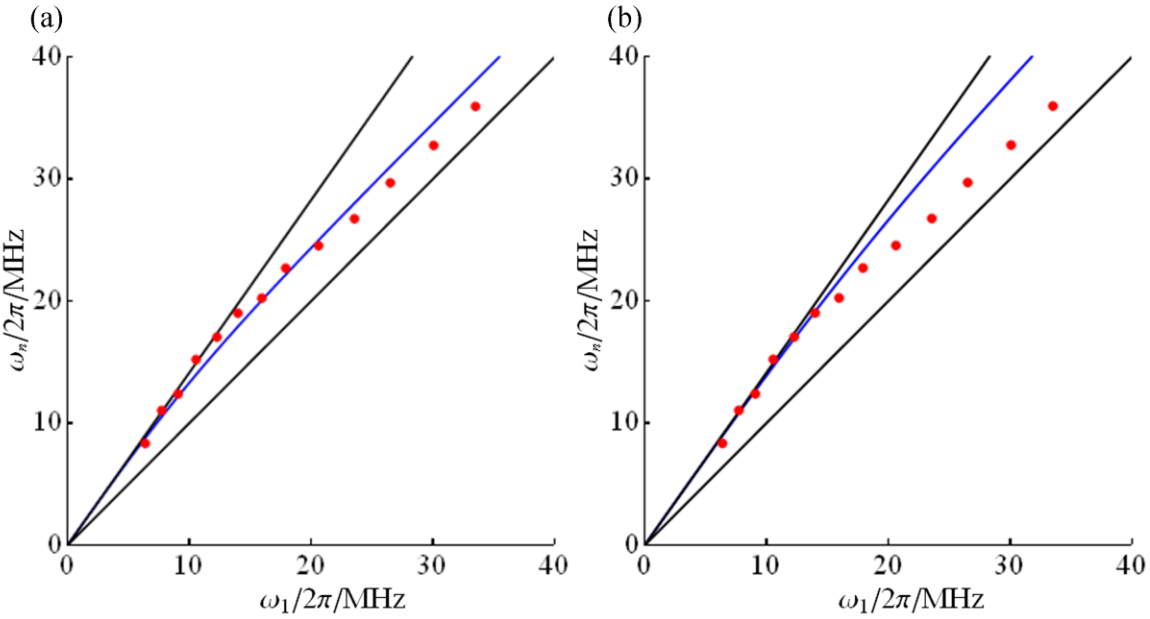

Figure S7. Nutation behaviour as a function of the microwave irradiation strength $\omega_1/2\pi$ with the *X*-/*Y*-canonical orientations (a) and the *Z*-orientation (b) of biradical **1** in the toluene glass. The lines in blue denote the theoretical nutation frequencies and the solid circles in red denote the observed nutation frequencies for the resonance field at 344 mT. The theoretical nutation frequency with the *Z*-orientation can be calculated by using the difference between the eigenvalues λ_3 and λ_4 given in the text.

7. Q-band PEANUT spectrum of biradical 1

The significant difference of the nutation frequency between the canonical orientations discussed in the preceding section S6 was clearly detected in the Phase-inverted Echo-Amplitude detected NUTation (PEANUT) experiment, which is another version of pulse ESR based ESN spectroscopy implemented by Schweiger and Stoll [S4]. In this experiment, the pulse sequence described by Figure S8 is used. We have observed the nutation frequency from the dependence of the rotary echo intensity as a function of the second pulse duration time. At the halfway of the duration time, the phase of the second pulse is inverted. This technique is particularly useful for the systems with relatively long relaxation time because one can always observe the echo signal at the common time when the echo signal is not affected by the relaxation.

A time-domain spectrum of the PEANUT experiment on biradical **1** is shown in Figure S9(a). In this experiment, the nutation signal oscillates at the frequency of $2\omega_n$ and ω_n at the centre and both end of the time-domain spectrum. The Fourier transformation of the central signal in Figure S9(a) was carried out, giving in Figure S9(b). In the Q-band spectrum of biradical **1**, there appears the peak at the lower field near 1206 mT, which is assigned to the *Z*-canonical orientation, as depicted in Figure 2(a) in the text. The Q-band PEANUT spectroscopy of biradical **1** agrees with the details of the X-band ESN analysis given in the preceding section.

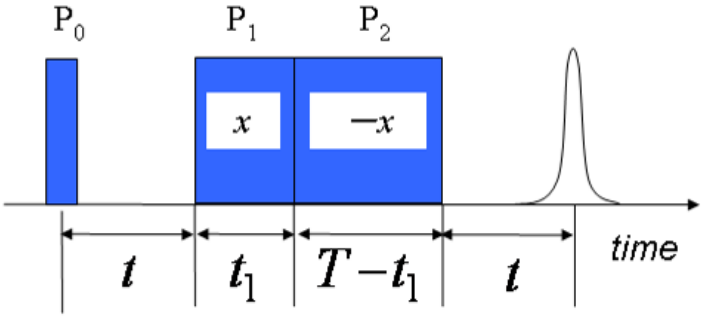

Figure S8. Pulse sequence for the PEANUT experiments. The parameters used for the experiments on biradical **1** are as follows: P_0 = 16 ns, $P_1 = t_1 = (8\times n)$ ns, $P_2 = (4088-8\times n)$ ns, t = 400 ns and T = 4088 ns.

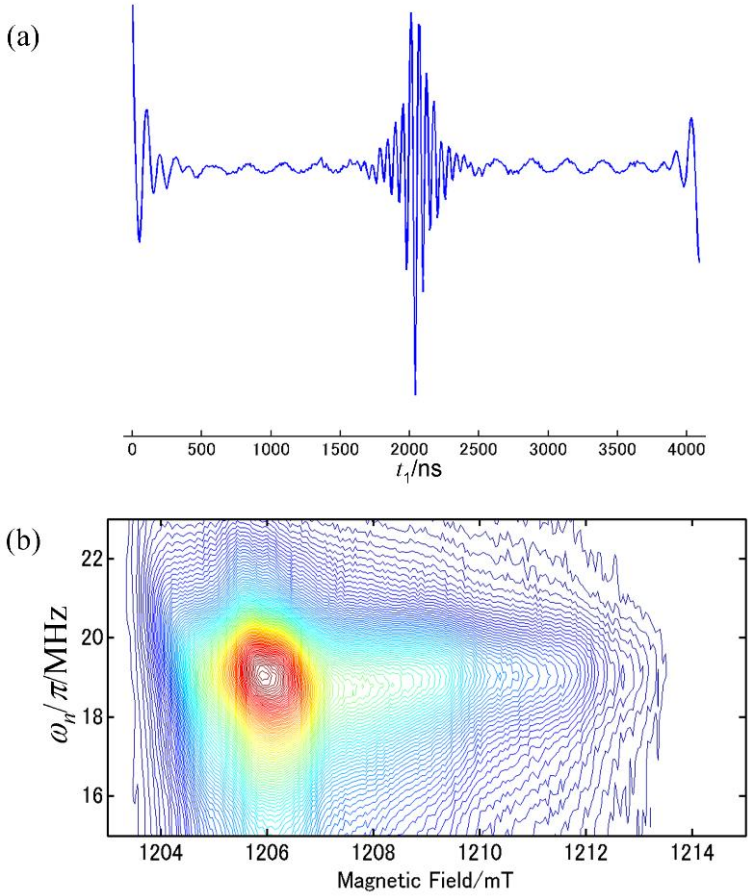

Figure S9. Q-band PEANUT spectra of biradical **1** in the toluene glass (T = 20 K, ν_{MW} = 33.897999 GHz). Note that the resonant microwave frequency is not the same as the one for the Q-band CW ESR spectrum. (a) The time-domain spectrum observed at B_0 = 1207.30 mT. (b) Contour plot of the frequency-domain spectra after the Fourier transformation of the signal appearing at the centre in (a).

8. Relaxation times, T_1 and T_2 of biradical 1 observed in the toluene glass

Relaxation times of biradical **1** were observed by the pulsed Q-band ESR spectrometer (ν_{MW} = 33.897999 GHz) at T = 20 K and the static magnetic field B_0 = 1206.37 mT. Figure S10 shows the T_1 curve obtained with the pulse sequence given in the inset. The observed T_1 decay curve was analysed in terms of a biexponential equation as follows:

$$a_1 \exp\left(-\frac{t}{T_1}\right) + a_2 \exp\left(-\frac{t}{T_1'}\right) + y_0 \qquad \text{(S1)}$$

The best-fit parameters are a_1 = −143902.13, a_2 = −117997.11, y_0 = 164104, T_1 = 4.0167843 ms and T_1' = 0.90103599 ms.

Figure S11 shows the behaviour of the relaxation time T_2 curve observed with the pulse sequence given in the inset. The signal oscillates at the period of about (250/2) ns. Fourier transformation of the oscillation gave only two peaks (see Fig. S12). The corresponding frequencies are consistent with the Larmor frequency of a deuterium nucleus ($|g_{D,n}\beta_n B_0/h|$ = 7.884 MHz at 1206.37 mT) and that of the second harmonics. The Larmor frequency of a proton nucleus and its second harmonic frequency have been observed in the electron spin echo envelope modulation (ESEEM) experiment of a biradical system. [S5] The oscillation observed at 20 K in the present work is attributable to the deuteruims of the methyl groups at the 2-, 2'-, 6- and 6'-positions of the piperidin rings of biradical **1**. The oscillation disappears when the pulse duration time becomes long. We analysed the T_2 decay curve in terms of the biexponential eq. S1 above with the following best-fit parameters: a_1 = 3691543.3, a_2 = −3493550.8, y_0 = −1117.4319, T_2 = 2.3148712 μs and T_2' = 2.1612062 μs, although the parameters did not satisfactorily reproduce the experimental curve as seen in Fig. S11. The relaxation study of T_2 suggests that biradical **1** in the toluene glass has the relaxation time long enough to perform the Q-band PEANUT experiments. A single crystal study of the deuterium hyperfine interactions of biradical **1** diluted in the corresponding bisketone at a desired concentration ratio is underway.

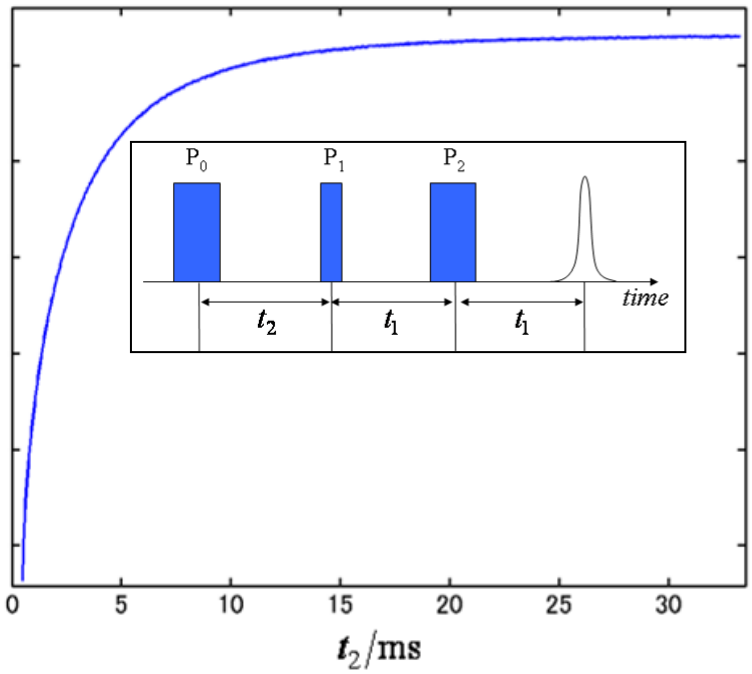

Figure S10. Spin-lattice relaxation time constant T_1 measurement with the pulse sequence given in the inset. The parameters of the sequence are $P_0 = P_2 = 32$ ns, $P_1 = 16$ ns, $t_1 = 800$ ns, $t_2 = (2000+30000\times n)$ ns, ($n = 0, 1, 2, \ldots, 1023$).

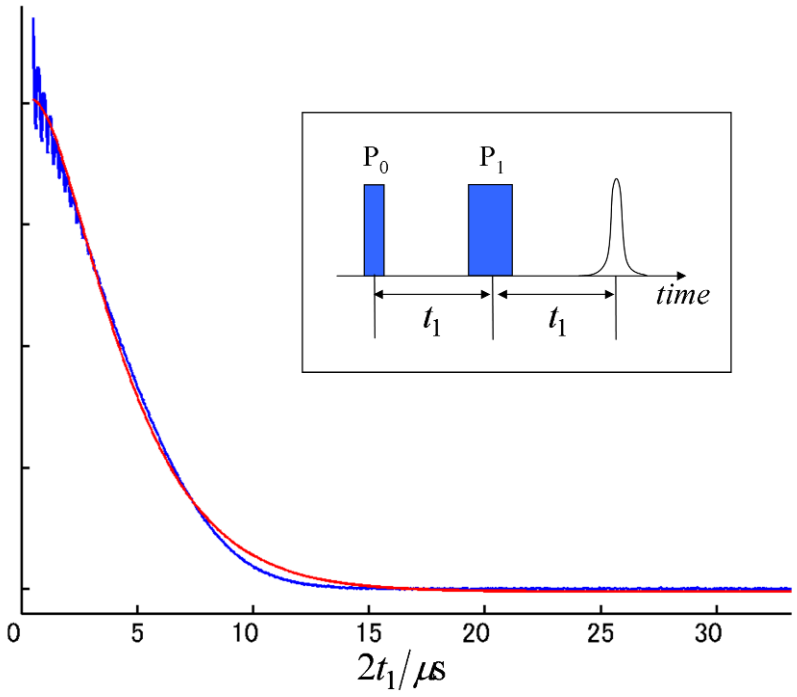

Figure S11. Spin-spin relaxation time constant T_2 measurement with the pulse sequence given in the inset. The parameters of the sequence are $P_0 = 16$ ns, $P_1 = 32$ ns, $t_1 = (250+16\times n)$ ns, ($n = 0, 1, 2, \ldots, 1023$).

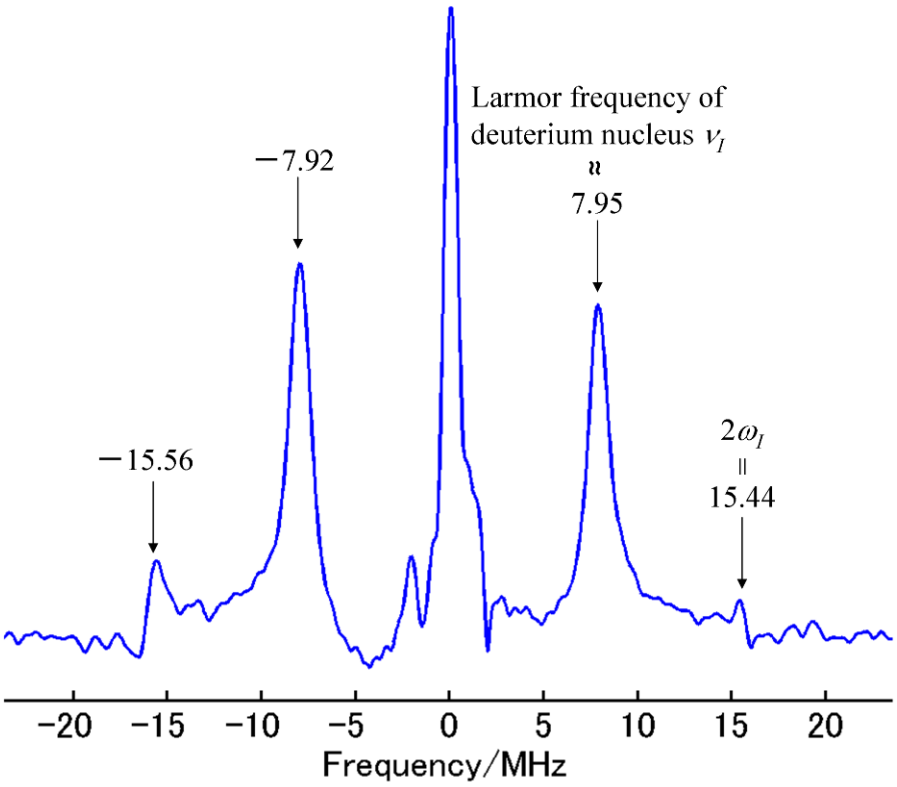

Figure S12. Fourier transformed spectrum of the oscillation in the spin-spin relaxation time T_2 curve showed in Fig. S11.

9. Optimised molecular structure of the isotope unlabelled biradical 2

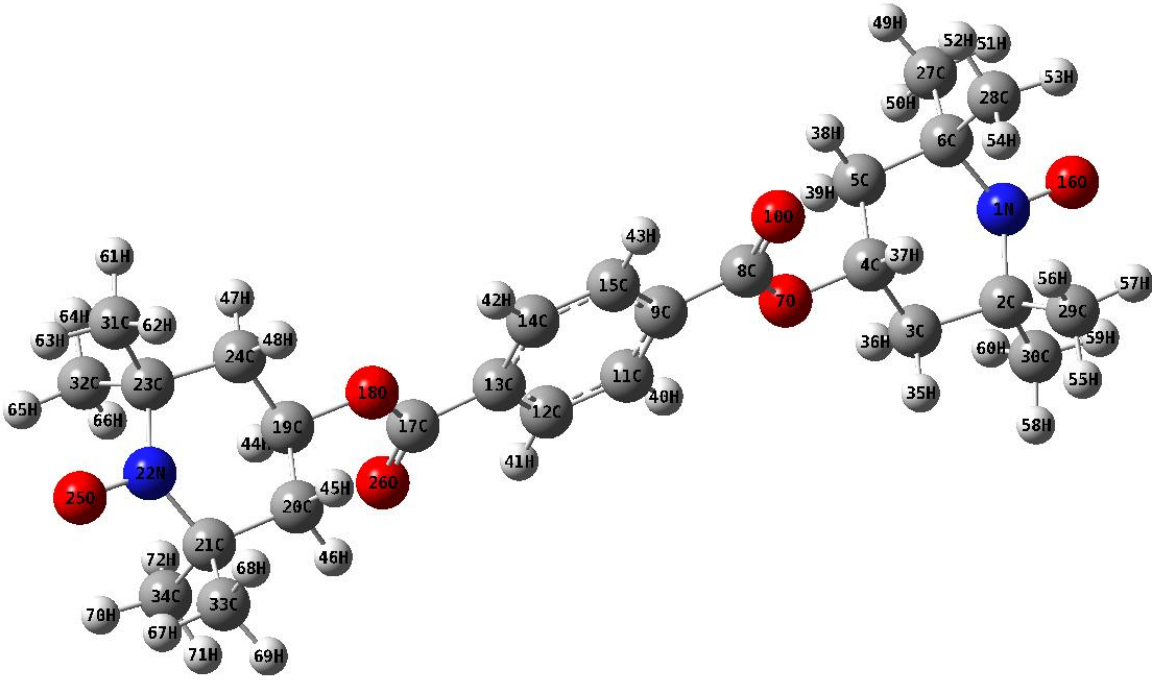

Figure S13. Optimised structure of the isotope unlabelled biradical **2**, in which the imaginary frequencies are zero, and the spin densities calculated by the level of UB3LYP/6-31G(d). The optimised structure has the symmetry of C_1. The molecular structure of the C_i symmetry was assumed at the transition state.

10. Cartesian coordinates and total energies for the optimised structure of biradical 2

The optimised molecular structure of biradical **2** (and **1**) was obtained at the level of UB3LYP/6-31G(d). The Cartesian coordinates of all the atoms are given in Table S2.

Table S2. Cartesian coordinates of the optimised structure for biradical **2** (and **1**), calculated at the level of UB3LYP/6-31G(d).[a]

atom	Coordinates /Å		
	X	Y	Z
1N	7.831938	−0.022985	−0.397395
2C	7.285113	−1.326436	0.112104
3C	5.760410	−1.387001	−0.115348
4C	5.051546	−0.102809	0.286847
5C	5.588217	1.062576	−0.536919
6C	7.100926	1.289613	−0.340752
7O	3.640140	−0.303446	0.006039
8C	2.764516	0.464241	0.693742
9C	1.345629	0.171071	0.330721
10O	3.096530	1.297568	1.514954
11C	0.995173	−0.814902	−0.602817
12C	−0.343982	−1.043227	−0.900013
13C	−1.345176	−0.288599	−0.273584
14C	−0.994596	0.697706	0.659548
15C	0.344194	0.923257	0.959685
16O	9.112943	0.055731	−0.455883
17C	−2.764629	−0.578124	−0.637668
18O	−3.633335	0.240284	−0.001337
19C	−5.045468	0.056859	−0.288449
20C	−5.629024	−1.004784	0.637172
21C	−7.146690	−1.202997	0.445571
22N	−7.835816	0.129421	0.352604
23C	−7.240553	1.359395	−0.271916
24C	−5.718331	1.395336	−0.025563
25O	−9.119439	−0.095220	−0.395173
26O	−3.101946	−1.445893	−1.419895
27C	7.638612	2.155313	−1.492039
28C	7.404138	1.985347	1.003961
29C	7.646622	−1.482216	1.605060
30C	7.963293	−2.447490	−0.692483

31C	−7.894148	2.573791	0.408218
32C	−7.575212	1.378785	−1.778912
33C	−7.724086	−1.924937	1.674306
34C	−7.458590	−2.027390	−0.822035
35H	5.353638	−2.237583	0.443290
36H	5.555721	−1.571718	−1.177599
37H	5.145060	0.099317	1.356218
38H	5.059188	1.984067	−0.274697
39H	5.382556	0.850451	−1.593971
40H	1.771601	−1.394923	−1.088063
41H	−0.636488	−1.802401	−1.617529
42H	−1.770859	1.279410	1.142938
43H	0.636550	1.680065	1.679732
44H	−5.128954	−0.246571	−1.334455
45H	−5.426162	−0.697049	1.671004
46H	−5.127136	−1.963980	0.473881
47H	−5.276653	2.174011	−0.657734
48H	−5.522177	1.677225	1.016806
49H	7.108317	3.113649	−1.510445
50H	7.487707	1.656010	−2.454881
51H	8.706695	2.340908	−1.365676
52H	7.016203	3.009670	0.990096
53H	8.486274	2.022079	1.156991
54H	6.950374	1.470300	1.855681
55H	7.398784	−2.493191	1.947417
56H	7.112607	−0.771543	2.242880
57H	8.720405	−1.322626	1.735816
58H	7.569751	−3.419402	−0.375187
59H	9.043185	−2.431299	−0.535803
60H	7.769158	−2.326724	−1.763349
61H	−7.463874	3.497712	0.006621
62H	−7.720870	2.551158	1.489163
63H	−8.971395	2.576529	0.233752
64H	−7.292688	2.344378	−2.213077
65H	−8.651119	1.236765	−1.912331
66H	−7.052069	0.595057	−2.335059
67H	−8.795814	−2.091269	1.552197
68H	−7.568985	−1.330726	2.580955

69H	−7.224087	−2.891145	1.802501
70H	−8.539261	−2.039659	−0.988750
71H	−7.111123	−3.058161	−0.692578
72H	−6.973482	−1.623821	−1.715644

[a] The atomic numbering is given in Figure S12. *E*(UB3LYP/6-31G(d)) = −1574.43000424 a.u..

11. Quantum chemical calculations for the zerofield tensor and the exchange coupling J_{12} of biradical 2

Quantum chemical calculations of the zerofield splitting tensor for biradical **1** were carried out by using the following McWeeny-Mizuno's equation (S2), which gives the contribution from the spin dipolar interaction with the help of ROB3LYP/EPR-Ⅱ[S6-S10]:

$$D_{ij}^{SS} = \frac{\alpha^2}{4S(2S-1)} \sum_{\mu\nu\kappa\lambda} \left(\rho_{\mu\nu}^{\alpha-\beta} \rho_{\kappa\lambda}^{\alpha-\beta} - \rho_{\mu\lambda}^{\alpha-\beta} \rho_{\kappa\nu}^{\alpha-\beta} \right) \times \int \mu^*(r_1) \kappa^*(r_1) \left(\frac{r_{12}^2 \delta_{ij} - 3(r_{12})_i (r_{12})_j}{r_{12}^5} \right) \nu(r_1) \lambda(r_1) dr_1 dr_2 \qquad \text{(S2)}$$

The calculation of the zerofield splitting tensor (**D**) was made for the molecular structure optimised by the level of UB3LYP/6-31G(d), as shown in the preceding section S10. We obtained the theoretical values of $D = -0.000558$ cm^{-1} $= -16.7_3$ MHz ($D_{12} = 2\times D = -33.4_6$ MHz), $|E| \simeq 2.79\times10^{-8}$ cm^{-1} and $|E/D| = 5\times10^{-5}$. The directions of the principal values of the theoretical **D** tensor are depicted in Figure S14. The principal axis for D_{ZZ}, i.e. D is parallel to the direction connecting the two N-O bonds. The theoretical **D** tensor is axial, suggesting that the point dipole–dipole approximation is valid in biradical **1** and **2**. The theoretical D value agrees well with the experimental one, suggesting that the contribution from the spin–orbit interactions is negligible in biradical **1** and **2**.

We attempted to calculate the J_{12} value of biradical **1** as a weakly exchange-coupled chemical entity by the broken-symmetry method [S11]. The equation for the theoretical J_{12} value is described by

$$J_{12} = \left\langle S^2 \right\rangle_{HS} \cdot J = \left\langle S^2 \right\rangle_{HS} \cdot \frac{E_{BS} - E_{HS}}{\left\langle S^2 \right\rangle_{HS} - \left\langle S^2 \right\rangle_{BS}} \qquad \text{(S3)}$$

where $\langle S^2 \rangle_{HS}$ and $\langle S^2 \rangle_{BS}$ denote the expectation value for the spin quantum number of the triplet state and the open-shell singlet state, respectively. E_{HS} and E_{BS} denote the energy of the triplet state and the open-shell singlet state, respectively. These values were calculated by the DFT calculations at the level of UB3LYP/6-31G(d) for the triplet state and B3LYP/6-31G(d) for the open-shell singlet state. The convergence condition of SCF had to be strict for both the energies of E_{HS} and E_{BS} [S12]. We obtained the following values: $\langle S^2 \rangle_{HS} = 2.0074$, $\langle S^2 \rangle_{BS} = 1.0074$, $E_{HS} = -1574.43000423684$ a.u., $E_{BS} = -1574.43000423646$ a.u. and $J_{12} = 3.8\times10^{-10}$ a.u. = 5.019061851 MHz. We have noted that strictly speaking the theoretical J_{12} value is be-

yond the current accuracy (one order of the magnitude greater than the obtained J_{12} value, which is evaluated on the basis of the current computation resource) of the DFT calculations. We can conclude, nevertheless, that the J_{12} value of biradical **2 (**and **1**) is small, requiring further improvement of the DFT calculations for such small exchange couplings.

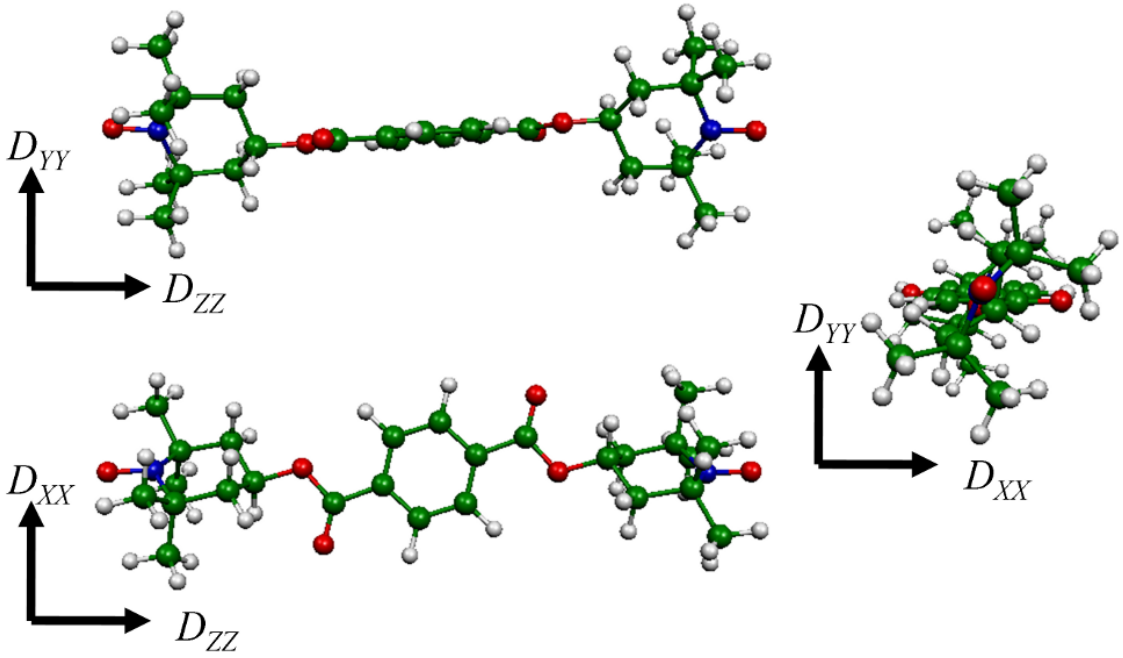

Figure S14. Principal axes of the zeofield splitting tensor for biradical **2**, calculated by McWeeny-Mizuno's equation for the spin dipolar interaction. The principal axis of D_{ZZ} is along the line connecting the two nitroxide sites. The principal value for D_{XX} is equivalent to that for D_{YY}, giving the axial symmetry of the tensor. The molecular structure was optimised by the level of UB3LYP/6-31G(d) using Gaussian 03 software [S12].

12. Possible conformations of biradical 2 (and 1).

We have examined whether there are any other optimised structures for biradical **2** (**1**) in addition to the structure discussed in Section S10. The possible structures can be classified into the three following categories: (i) whether the C-O double bonds point in the same direction with respect to the principal axis of D_{zz} or not (cis-trans isomers), (ii) whether the hydrogen atom which is bonded to the 4-position carbon of the TEMPO moiety points in the same direction as the C-O double bond of the ester bond or not, (iii) in the case that the hydrogen atoms point in the same direction as the C-O double bond of the ester bonds in (ii), whether these hydrogen atoms are in the same side with respect to the phenyl ring or not. Summary of the classified conformations and the corresponding optimised energies is given in Table S3 and Figure S15.

Among those structures, the ones denoted by ① – ④ are likely in the toluene frozen glass in terms of the optimised energy. The Cartesian coordinates of all the atoms of the structures ① – ④ (see S10 for the structure ④) are given in Tables S4 – 6.

In addition, it is conceivable that the molecule undergoes the boat conformation of the TEMPO ring. The DFT calculations cannot afford any boat conformation.

Table S3. Summary of the possible optimised conformations and their energies of biradical **2** (and **1**), as calculated at the level of UB3LYP/6-31G(d).

Category				Energy/a.u.
(i)	(ii)		(iii)	
	Site 1	Site 2		
cis	Same	Same	Same	−1574.43000658 ①
	Same	Same	Different	−1574.42999346 ②
	Same	Different	−	−1574.42512319
	Different	Different	−	−1574.42026851
trans	Same	Same	Same	−1574.43008010 ③
	Same	Same	Different	−1574.43000424 ④
	Same	Different	−	−1574.42530533
	Different	Different	−	−1574.42045082

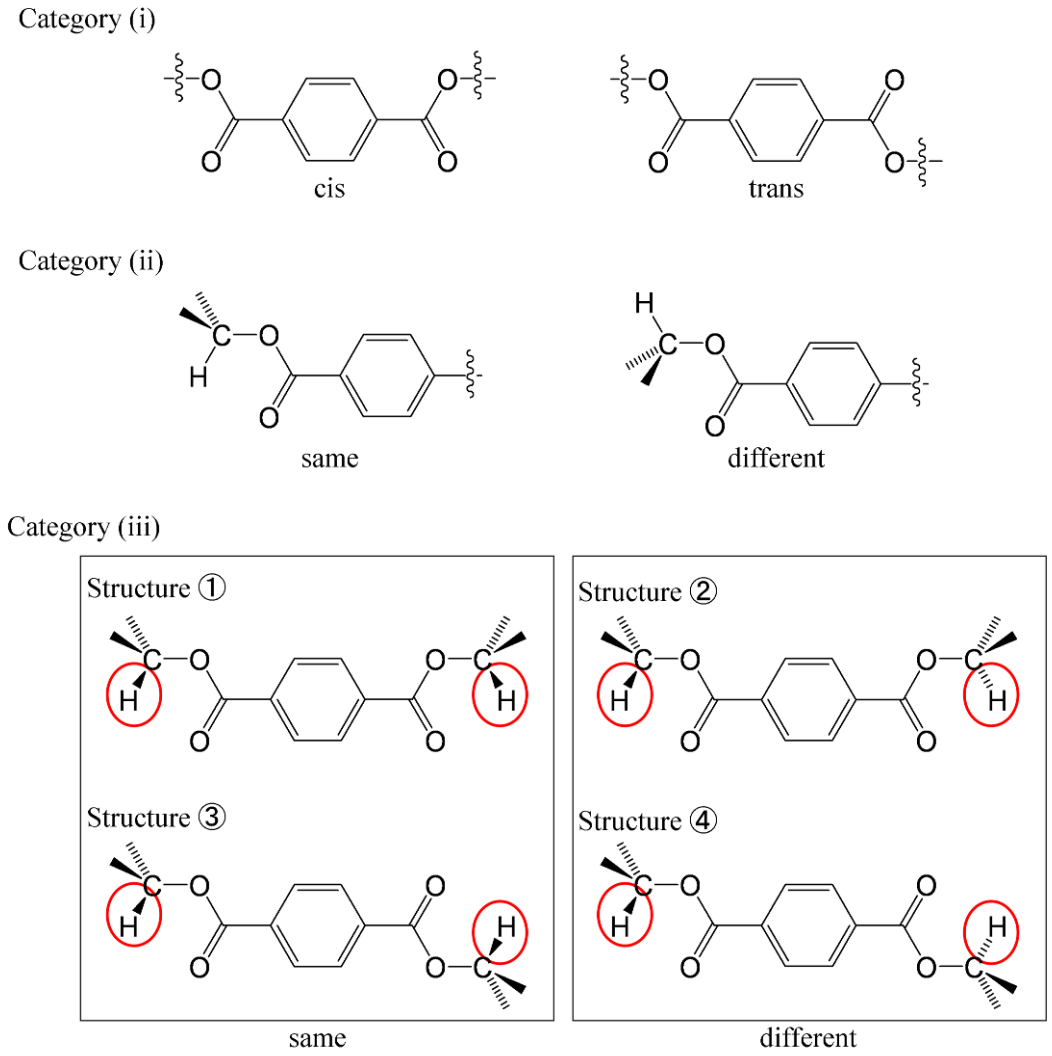

Figure S15. Classification of the structures for biradical **1** (and **2**) given in Table S3. The four oxygen atoms lie in the plane of this paper.

Table S4. Cartesian coordinates of the optimised structure ① for biradical **2** (and **1**), as calculated at the level of UB3LYP/6-31G(d).[b]

Atom	Coordinates /Å		
	X	Y	Z
1N	−7.823482	−0.312033	0.322521
2C	−7.295952	−0.840361	−0.981429
3C	−5.768886	−1.038452	−0.894120
4C	−5.054828	0.142689	−0.255190
5C	−5.569027	0.349660	1.165507
6C	−7.083146	0.638902	1.220568
7O	−3.641694	−0.193066	−0.228893
8C	−2.766929	0.838011	−0.198514
9C	−1.346596	0.375818	−0.193683
10O	−3.100692	2.007293	−0.182909
11C	−0.997265	−0.982333	−0.194589
12C	0.342892	−1.353102	−0.193307
13C	1.346608	−0.374939	−0.194522
14C	0.997279	0.983209	−0.192650
15C	−0.342882	1.353976	−0.190539
16O	−9.102688	−0.308493	0.442093
17C	2.766923	−0.837158	−0.200374
18O	3.641740	0.193932	−0.228833
19C	5.054861	−0.141907	−0.255680
20C	5.769159	1.040504	−0.891978
21C	7.296207	0.842341	−0.979504
22N	7.823508	0.311061	0.323398
23C	7.082888	−0.641785	1.219180
24C	5.568831	−0.352095	1.164598
25O	9.102685	0.306988	0.443142
26O	3.100626	−2.006489	−0.187107
27C	−7.594185	0.399420	2.650842
28C	−7.401727	2.090240	0.801243
29C	−7.682278	0.129971	−2.118589
30C	−7.970563	−2.200318	−1.225713
31C	7.593810	−0.405746	2.650054
32C	7.401236	−2.092196	0.796492
33C	7.971121	2.202681	−1.220741
34C	7.682467	−0.125634	−2.118717

35H	−5. 378285	−1. 219720	−1. 901884
36H	−5. 549036	−1. 933035	−0. 297585
37H	−5. 161753	1. 055375	−0. 845441
38H	−5. 036852	1. 179386	1. 641555
39H	−5. 347671	−0. 559400	1. 739262
40H	−1. 775210	−1. 736958	−0. 196145
41H	0. 634459	−2. 397960	−0. 193620
42H	1. 775226	1. 737836	−0. 192690
43H	−0. 634446	2. 398833	−0. 188687
44H	5. 161763	−1. 053308	−0. 847914
45H	5. 549365	1. 933862	−0. 293588
46H	5. 378747	1. 223942	−1. 899422
47H	5. 036433	−1. 182775	1. 638716
48H	5. 347626	0. 555723	1. 740367
49H	−7. 053134	1. 048004	3. 348402
50H	−7. 434141	−0. 641935	2. 949603
51H	−8. 661980	0. 641935	2. 718327
52H	−7. 007434	2. 789669	1. 546481
53H	−8. 485762	2. 219538	0. 737771
54H	−6. 962978	2. 353275	−0. 165726
55H	−7. 452186	−0. 320781	−3. 090495
56H	−7. 149546	1. 083573	−2. 056454
57H	−8. 755939	0. 331935	−2. 072776
58H	−7. 589790	−2. 638902	−2. 154571
59H	−9. 052649	−2. 082446	−1. 303949
60H	−7. 758197	−2. 891030	−0. 402980
61H	7. 052643	−1. 055969	3. 345997
62H	7. 433823	0. 634898	2. 951310
63H	8. 661581	−0. 621878	2. 717121
64H	7. 006653	−2. 793330	1. 539976
65H	8. 485249	−2. 221603	0. 732892
66H	6. 962624	−2. 352822	−0. 171187
67H	9. 053195	2. 084751	−1. 299035
68H	7. 758760	2. 891641	−0. 396538
69H	7. 590578	2. 643341	−2. 148707
70H	8. 756086	−0. 327891	−2. 073255
71H	7. 452548	0. 327252	−3. 089677
72H	7. 149509	−1. 079249	−2. 058694

[b] The atomic numbering is given in Figure S12. *E*(UB3LYP/6-31G(d)) = −1574.43008010 a.u..

Table S5. Cartesian coordinates of the optimised structure ② for biradical **2** (and **1**), as calculated at the level of UB3LYP/6-31G(d).[c]

atom	Coordinates /Å		
	X	Y	Z
1N	7.430128	0.903381	0.680150
2C	6.776380	1.696670	−0.415343
3C	5.255747	1.439339	−0.418901
4C	4.901853	−0.34443	−0.290869
5C	5.456212	−0.588656	1.016855
6C	6.990188	−0.463659	1.123336
7O	3.450884	−0.107379	−0.285880
8C	2.890612	−1.273203	−1.681795
9C	1.398044	−1.219984	−0.655002
10O	3.530231	−2.248727	−1.024732
11C	0.694769	−2.364291	−1.057009
12C	−0.694677	−2.364365	−1.056896
13C	−1.398010	−1.220129	−0.654789
14C	−0.695799	−0.076577	−0.249339
15C	0.695777	−0.076507	−0.249440
16O	8.657131	1.198029	0.921709
17C	−2.890578	−1.273500	−0.681359
18O	−3.450904	−0.107612	−0.285712
19C	−4.901879	−0.034745	−0.290694
20C	−5.456148	−0.588184	1.017398
21C	−6.990137	−0.463239	1.123815
22N	−7.430042	0.903667	0.680138
23C	−6.776489	1.696242	−0.415993
24C	−5.255842	1.438955	−0.419564
25O	−8.656967	1.198589	0.921781
26O	−3.530149	−2.249191	−1.023909
27C	7.410537	−0.618080	2.594321
28C	7.710315	−1.532470	0.273284
29C	7.422175	1.327658	−1.768290
30C	7.038485	3.182233	−0.117855
31C	−7.038590	3.181994	−0.119426

32C	−7. 422429	1. 326420	−1. 768654
33C	−7. 410538	−0. 617171	2. 594823
34C	−7. 710217	−1. 532383	0. 274142
35H	4. 829292	1. 854225	−1. 339298
36H	4. 793144	1. 974035	0. 420484
37H	5. 254901	−0. 617903	−1. 144265
38H	5. 181899	−1. 642970	1. 123851
39H	4. 985043	−0. 038374	1. 841424
40H	1. 256125	−3. 239425	−1. 366412
41H	−1. 255989	−3. 239563	−1. 366199
42H	−1. 242783	0. 805535	0. 062627
43H	1. 242717	0. 805659	0. 062454
44H	−5. 254930	−0. 618743	−1. 143717
45H	−4. 985035	−0. 037295	1. 841588
46H	−5. 181712	−1. 642396	1. 125094
47H	−4. 829485	1. 853335	−1. 340235
48H	−4. 793191	1. 974137	0. 419482
49H	7. 074762	−1. 589852	2. 972262
50H	6. 961296	0. 168330	3. 209909
51H	8. 495549	−0. 552610	2. 692404
52H	7. 537021	−2. 527115	0. 698349
53H	8. 785408	−1. 332586	0. 275408
54H	7. 362129	−1. 549641	−0. 763613
55H	7. 076744	2. 015011	−2. 548663
56H	7. 178657	0. 309638	−2. 086520
57H	8. 509254	1. 411827	−1. 685319
58H	6. 547344	3. 802032	−0. 875978
59H	8. 109507	3. 391588	−0. 125065
60H	6. 641035	3. 455857	0. 865115
61H	−6. 547669	3. 801301	−0. 878090
62H	−6. 640908	3. 456307	0. 863259
63H	−8. 109625	3. 391288	−0. 126507
64H	−7. 077586	2. 013741	−2. 549314
65H	−8. 509534	1. 410032	−1. 685447
66H	−7. 178414	0. 308462	−2. 086687
67H	−8. 495395	−0. 549434	2. 693003
68H	−6. 959555	0. 168114	3. 210582
69H	−7. 076757	−1. 589745	2. 972454

70H	−8. 785495	−1. 333487	0. 277473
71H	−7. 535547	−2. 527025	0. 698645
72H	−7. 363181	−1. 548851	−0. 763143

[c] The atomic numbering is given in Figure S12. *E*(UB3LYP/6-31G(d)) = −1574.43000658 a.u..

Table S6. Cartesian coordinates of the optimised structure ③ for biradical **2** (and **1**), as calculated at the level of UB3LYP/6-31G(d).[d]

atom	Coordinates /Å		
	X	Y	Z
1N	−7. 450516	1. 074193	−0. 201397
2C	−6. 751032	1. 444376	1. 075804
3C	−5. 233399	1. 210522	0. 934522
4C	−4. 896192	−0. 127640	0. 294975
5C	−5. 501827	−0. 201124	−1. 102380
6C	−7. 037373	−0. 054325	−1. 104172
7O	−3. 447019	−0. 189442	0. 209563
8C	−2. 885835	−1. 419451	0. 162555
9C	−1. 395766	−1. 358696	0. 079010
10O	−3. 523044	−2. 454698	0. 188140
11C	−0. 693566	−2. 571494	0. 038558
12C	0. 693608	−2. 571468	−0. 038920
13C	1. 395774	−1. 358644	−0. 079153
14C	0. 694720	−0. 145333	−0. 039778
15C	−0. 694746	−0. 145359	0. 039856
16O	−8. 683054	1. 427848	−0. 281258
17C	2. 885847	−1. 419340	−0. 162715
18O	3. 446997	−0. 189311	−0. 209577
19C	4. 896161	−0. 127474	−0. 295014
20C	5. 233334	1. 210928	−0. 934078
21C	6. 750956	1. 444807	−1. 075433
22N	7. 450635	1. 073980	0. 201470
23C	7. 037428	−0. 054694	1. 104015
24C	5. 501877	−0. 201432	1. 102278
25O	8. 683266	1. 427347	0. 281191
26O	3. 523089	−2. 454560	−0. 188510
27C	−7. 510878	0. 305805	−2. 522126
28C	−7. 735851	−1. 354094	−0. 650454

29C	−7. 349860	0. 628119	2. 241535
30C	−7. 013153	2. 939980	1. 318576
31C	7. 511018	0. 305058	2. 522039
32C	7. 735771	−1. 354418	0. 649943
33C	7. 013091	2. 940513	−1. 317526
34C	7. 349606	0. 629084	−2. 241641
35H	−4. 770300	1. 285805	1. 924982
36H	−4. 797561	2. 003922	0. 313972
37H	−5. 222829	−0. 970350	0. 908363
38H	−5. 240497	−1. 152970	−1. 575509
39H	−5. 055798	0. 601421	−1. 703706
40H	−1. 254052	−3. 499700	0. 069634
41H	1. 254121	−3. 499653	−0. 070162
42H	1. 240840	0. 790357	−0. 070819
43H	−1. 240892	0. 790309	0. 071070
44H	5. 222783	−0. 969955	−0. 908727
45H	4. 797574	2. 004093	−0. 313171
46H	4. 770136	1. 286621	−1. 924459
47H	5. 240554	−1. 153421	1. 575118
48H	5. 055895	0. 600932	1. 703880
49H	−7. 198589	−0. 475219	−3. 223831
50H	−7. 076012	1. 257351	−2. 845541
51H	−8. 597961	0. 397767	−2. 551452
52H	−7. 578293	−2. 142208	−1. 394842
53H	−8. 809993	−1. 173392	−0. 553309
54H	−7. 358068	−1. 723055	0. 307608
55H	−6. 968557	1. 004451	3. 197420
56H	−7. 105455	−0. 436497	2. 178914
57H	−8. 438329	0. 732453	2. 234455
58H	−6. 489656	3. 263437	2. 224932
59H	−8. 081623	3. 127454	1. 437389
60H	−6. 650780	3. 538045	0. 475918
61H	7. 198881	−0. 476204	3. 223548
62H	7. 076076	1. 256460	2. 845774
63H	8. 598093	0. 397125	2. 551271
64H	7. 577975	−2. 142787	1. 394010
65H	8. 809952	−1. 173855	0. 552996
66H	7. 358047	−1. 722946	−0. 308312

67H	8.081566	3.128004	−1.436255
68H	6.650735	3.538197	−0.474588
69H	6.489596	3.264405	−2.223727
70H	8.438047	0.733713	−2.234899
71H	6.967859	1.005589	−3.197280
72H	7.105524	−0.435616	−2.179227

[d] The atomic numbering is given in Figure S12. *E*(UB3LYP/6-31G(d)) = −1574.42999346 a.u.

13. Simulation of X- and Q-band random-orientation CW ESR spectra for the conformers

Figure S16 and S17 show the simulated spectra of X- and Q-band random orientation CW ESR spectra among the possible conformations discussed in the section S12, respectively. In the spectra (a)–(c), the additional signals appear, compared with the observed spectrum. These additional signals that are not seen in the observed spectrum are assigned to the additional canonical orientations which are due to the non-collinearity between the g- and *A*-tensors of each radical site. The comparison leads to the conclusion that the conformation ④ reproduces the observed spectrum arising from the collinearrity of the g- and *A*-tensors.

When executing the simulation, the *g*- and *A*-tensors undergo the transformation with the matrix U_{ij} in terms of the D_{12}-tensor as shown below;

$$U_{11} = \begin{pmatrix} 0.2978 & 0.3720 & 0.8792 \\ 0.0348 & -0.9246 & 0.3794 \\ 0.9540 & -0.0824 & -0.2883 \end{pmatrix}, \quad U_{12} = \begin{pmatrix} 0.2914 & -0.3720 & 0.8813 \\ 0.0348 & 0.9248 & 0.3789 \\ -0.9560 & -0.0797 & 0.2825 \end{pmatrix}$$

$$\begin{array}{c} \\ D_x \\ D_y \\ D_z \end{array} \begin{array}{c} \begin{array}{ccc} x_1 & y_1 & z_1 \end{array} \\ \begin{pmatrix} 72.67° & 68.16° & 28.45° \\ 88.01° & 157.61° & 67.70° \\ 17.45° & 94.57° & 106.76° \end{pmatrix} \end{array}, \quad \begin{array}{c} \\ D_x \\ D_y \\ D_z \end{array} \begin{array}{c} \begin{array}{ccc} x_2 & y_2 & z_2 \end{array} \\ \begin{pmatrix} 73.06° & 111.84° & 28.20° \\ 88.01° & 22.36° & 67.73° \\ 162.94° & 94.57° & 73.59° \end{pmatrix} \end{array}$$

$$U_{21} = \begin{pmatrix} 0.2662 & 0.5497 & 0.7918 \\ -0.0294 & 0.8257 & -0.5633 \\ -0.9635 & 0.1267 & 0.2360 \end{pmatrix}, \quad U_{22} = \begin{pmatrix} 0.2840 & 0.5764 & 0.7663 \\ 0.0391 & -0.8055 & 0.5914 \\ 0.9580 & -0.1380 & -0.2513 \end{pmatrix}$$

$$\begin{array}{c} \\ D_x \\ D_y \\ D_z \end{array} \begin{array}{c} \begin{array}{ccc} x_1 & y_1 & z_1 \end{array} \\ \begin{pmatrix} 74.56° & 56.65° & 37.65° \\ 91.68° & 34.34° & 124.28° \\ 164.47° & 82.72° & 76.35° \end{pmatrix} \end{array}, \quad \begin{array}{c} \\ D_x \\ D_y \\ D_z \end{array} \begin{array}{c} \begin{array}{ccc} x_2 & y_2 & z_2 \end{array} \\ \begin{pmatrix} 73.50° & 54.80° & 39.98° \\ 87.76° & 143.66° & 53.74° \\ 16.66° & 97.93° & 104.55° \end{pmatrix} \end{array}$$

$$U_{31} = \begin{pmatrix} 0.0462 & -0.5887 & -0.8070 \\ 0.0939 & -0.8017 & 0.5902 \\ -0.9945 & -0.1031 & 0.0183 \end{pmatrix}, \quad U_{32} = \begin{pmatrix} -0.0383 & 0.5167 & 0.8553 \\ 0.0922 & -0.8505 & 0.5179 \\ 0.9950 & 0.0987 & -0.0150 \end{pmatrix}$$

$$\begin{array}{c} \\ D_x \\ D_y \\ D_z \end{array} \begin{array}{c} \begin{array}{ccc} x_1 & y_1 & z_1 \end{array} \\ \begin{pmatrix} 87.35° & 126.07° & 143.80° \\ 84.61° & 143.29° & 53.83° \\ 173.99° & 95.92° & 88.95° \end{pmatrix} \end{array}, \quad \begin{array}{c} \\ D_x \\ D_y \\ D_z \end{array} \begin{array}{c} \begin{array}{ccc} x_2 & y_2 & z_2 \end{array} \\ \begin{pmatrix} 92.20° & 58.89° & 31.21° \\ 84.71° & 148.27° & 58.81° \\ 5.73° & 84.34° & 90.86° \end{pmatrix} \end{array}$$

$$U_{41} = \begin{pmatrix} 0.0455 & -0.5530 & 0.8319 \\ 0.0494 & -0.8305 & -0.5548 \\ 0.9977 & 0.0663 & -0.0105 \end{pmatrix}, \quad U_{42} = \begin{pmatrix} -0.0306 & -0.4682 & -0.8831 \\ -0.0157 & -0.8832 & 0.4688 \\ -0.9994 & 0.0282 & 0.0197 \end{pmatrix}$$

$$\begin{array}{c} \\ D_x \\ D_y \\ D_z \end{array} \begin{array}{c} \begin{array}{ccc} x_1 & y_1 & z_1 \end{array} \\ \begin{pmatrix} 87.39° & 123.57° & 33.71° \\ 87.17° & 146.15° & 123.70° \\ 3.89° & 86.20° & 90.60° \end{pmatrix} \end{array}, \quad \begin{array}{c} \\ D_x \\ D_y \\ D_z \end{array} \begin{array}{c} \begin{array}{ccc} x_2 & y_2 & z_2 \end{array} \\ \begin{pmatrix} 91.75° & 117.92° & 152.02° \\ 90.90° & 152.03° & 62.04° \\ 178.02° & 88.38° & 88.87° \end{pmatrix} \end{array}$$

where i and j of U_{ij} denote the number corresponding to the conformation ① – ④ and the label of each radical site, respectively. These matrices represent the angles between the principal axis of the D_{12}-tensor (D_x, D_y and D_z) and the principal axis of the g- and A-tensors with the calculated arc cosine of each element of U_{ij}. In the spectral simulation, the fixed J_{12} value of -1.0 MHz was chosen and the D_{12} value used was calculated by the point dipole approximation (g = 2.0101) with the spin distance between the midpoints of the N-O bonds of the optimised structures, which are given in Section 12. The point dipole approximation for biradical **1** has been well established in this work.

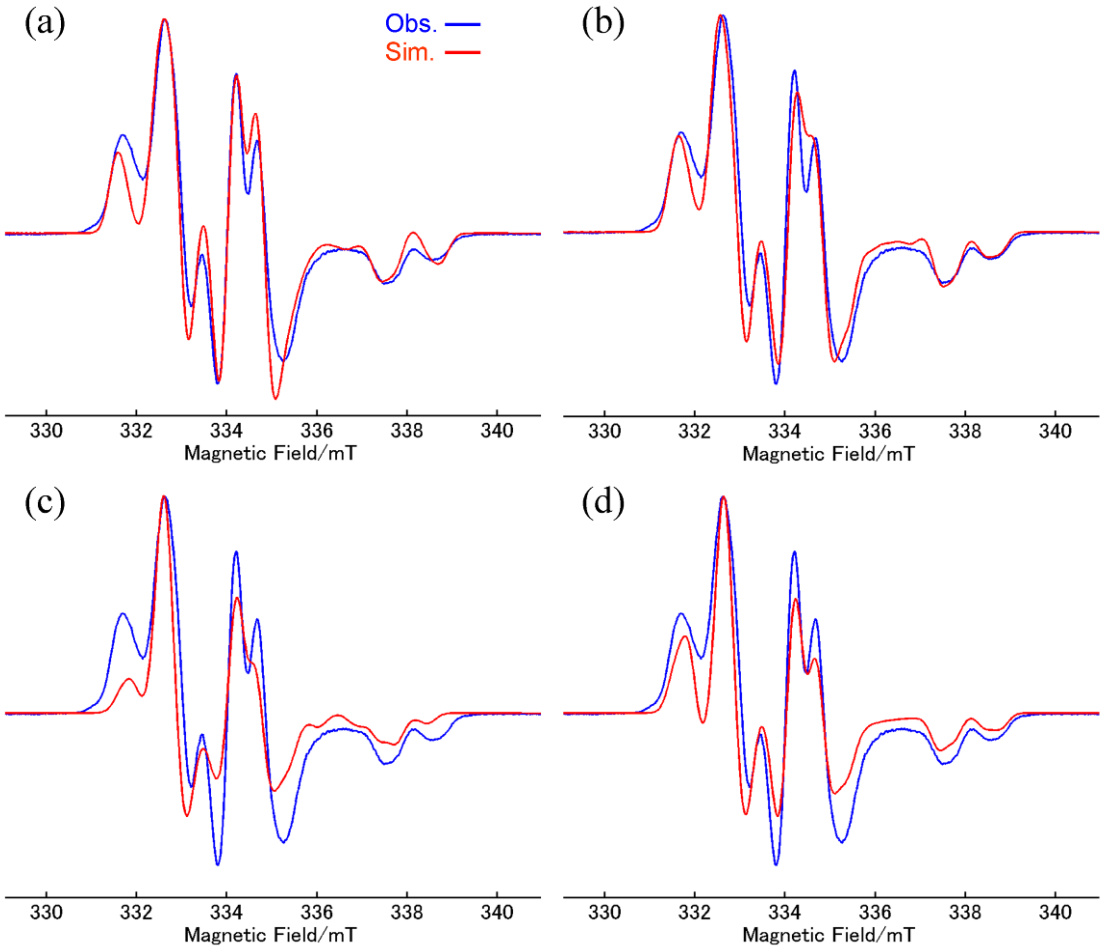

Figure S16. Simulation of the random-orientation X-band CW ESR spectra based on the optimised structures discussed in Section S12; (a) conformation ① (D_{12} = −37.79 MHz), (b) conformation ② (D_{12} = −37.42 MHz), (c) conformation ③ (D_{12} = −32.38 MHz), (d) conformation ④ (D_{12} = −32.25 MHz).

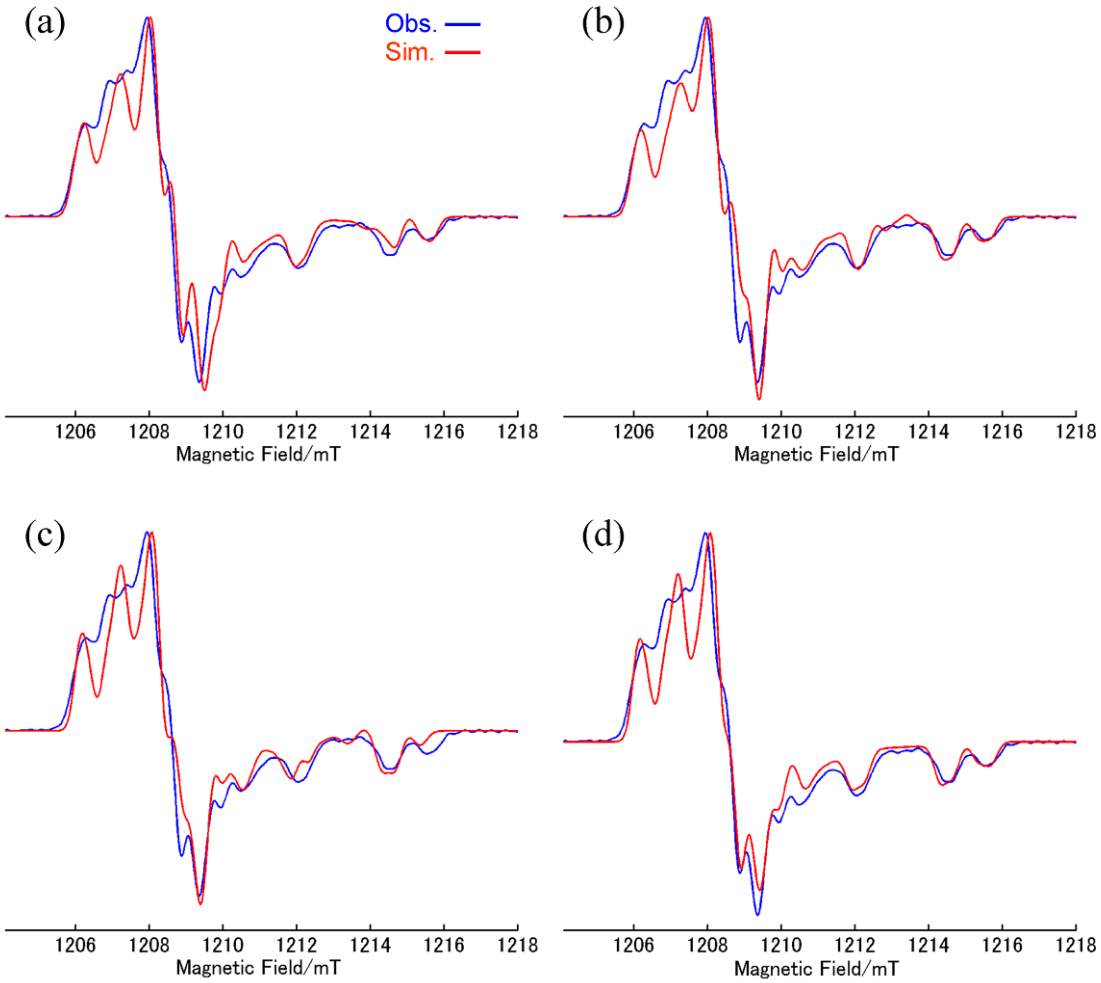

Figure S17. Simulation of the random-orientation Q-band CW ESR spectra based on the optimised structures discussed in the section S12; (a) conformation ① (D_{12} = −37.79 MHz), (b) conformation ② (D_{12} = −37.42 MHz), (c) conformation ③ (D_{12} = −32.38 MHz), (d) conformation ④ (D_{12} = −32.25 MHz).

14. Contribution from the forbidden transition due to nuclear spins

Prior to the numerical calculations of the nutation frequencies with hyperfine interactions taken into account, the transition moments with nuclear spin effects incorporated were calculated in terms of the spin Hamiltonian below with a particular orientation of the static magnetic field, i.e. B_0 = 0.341 mT. The experimentally determined magnetic parameters, which were based on the 2D-ESN measurements and the simulation of the CW ESR spectra were employed;

$$H = H_1 + H_2 + H_{12}$$

$$H_1 = g_{1,i}\beta B_0 S_{1i} + h\mathbf{I}_1 \cdot \mathbf{A}_1 \cdot \mathbf{S}_1 - g_{^{14}\mathrm{N}}\beta_n B_0 \cdot \mathbf{I}_1 + h\mathbf{I}_1 \cdot \mathbf{Q} \cdot \mathbf{I}_1$$

$$H_2 = g_{2,i}\beta B_0 S_{2i} + h\mathbf{I}_2 \cdot \mathbf{A}_2 \cdot \mathbf{S}_2 - g_{^{15}\mathrm{N}}\beta_n B_0 \cdot \mathbf{I}_2$$

$$H_{12} = h\left(\mathbf{S}_1 \cdot \mathbf{D}_{12} \cdot \mathbf{S}_2 + J_{12}\mathbf{S}_1 \cdot \mathbf{S}_2\right)$$

where *i* denotes the *x*-, *y*-, or *z*-direction.

When the principal axes of the magnetic tensors for each radical site are not coaxial and the static magnetic field is oriented toward the D_{zz} direction, the transition moment of the hyperfine forbidden transitions due to the change of the quantisation axis of nuclear spins was calculated to be significantly large. The maximum value is 0.1230, which amounts to nearly one third of the maximum of the allowed transition moment, 0.6875). When the static magnetic field is along the D_{xx} (or D_{yy}) direction, the forbidden transition whose moment is over 0.1 does not appear. This is due to the fact that the D_{12} tensor has the axial symmetry (E_{12} = 0).

On the other hand, when all the tensors are coaxial, the hyperfine forbidden transition moment ($\Delta M_{I1} = \Delta M_{I2} = \pm 1$) is extremely small (< 0.0006) while the hyperfine allowed transition ($\Delta M_{I1} = \Delta M_{I2} = 0$) amounts to 0.5515 at maximum, obtaining $\Delta M_I = 0$, where ΔM_I implies any change of the quantisation axis of the nuclear spins during the electron spin transition. We have carefully observed the nutation frequency throughout the magnetic field. It has turned out that in the present case of biradical **1** there has been significant departure of the observed nutation frequencies from the theoretical ones with the only four electronic spin states considered in the calculation. Quantitative analyses of the nutation behaviour of biradical 1 are given in Section 19.

15. Analysis of the 3-pulse ELDOR spectrum of biradical 1

The black line of Figure 7(a) in the main text indicates that the pulsed ELDOR spectrum after the base line correction was made in terms of the exponential decay based on the three dimensional homogenous spatial distribution. The pulse sequence used is shown in Fig. S1(c) with $\Delta\nu$ = 65 MHz at T = 20 K (the position of the observing and pumping pulses are given in the echo-detected field swept ESR spectrum; the inset of Fig. 7(a)). In order to derive the experimental D_{12} and J_{12} values, the Fourier transformation was carried out, obtaining the dipolar type spectrum shown in black in Fig. 7(b). Then, Tikhonov regularisation was applied to the base-line corrected ELDOR signal. The red lines in Fig. 7(a) and (b) denote the results with the regularisation parameter λ = 0.001. From Fig. 7(b), the values for $\nu_{\perp}$ and $\nu_{//}$ are determined to be 11.74 ± 0.535 MHz and −23.66 ± 0.805 MHz, respectively. These values lead the values for ν_D and ν_J by the following first-order equations [S13-15];

$$\nu_D = \frac{\nu_{\perp} - \nu_{\parallel}}{3} \quad , \qquad \nu_J = \frac{2\nu_{\perp} + \nu_{\parallel}}{3} \, .$$

We have obtained ν_D = 11.80 ± 0.45 MHz and ν_J = −0.06 ± 0.625 MHz, giving D_{12} = −35.40 ± 1.35 MHz and J_{12} = −0.06 ± 0.625 MHz. The values obtained by the ELDOR technique confirmed that the X-band pulse-based ESN spectroscopy combined with the CW ESR spectroscopy can afford to provide us with the reliable values within errors estimated quantitatively in this work.

16. Procedure for the numerical calculation of the nutation frequency as a function of microwave irradiation strength

(1) Calculate the spin Hamiltonians in the rotating frame, $H_{0,\,rot}$ and H'_{rot} which rotates with a frequency $\nu = (\omega_0/2\pi)\{1+\Delta g/(2g_1)\} + \Delta\omega/2\pi$, where $\omega_0/2\pi$ is given by $g_1\beta B_0/h$ = 10 GHz.

(2) For a given value of $\omega_1/2\pi$, calculate $\rho(t_0 = 0)$ using the third and fourth equations in Eq(4).

(3) Calculate the $I_1(t) = [tr((S_{1x} + S_{2x})\rho(t = t_0 + dt)) - \text{mean}(tr((S_{1x} + S_{2x})\rho(t = t_0 + dt)))]$ and $I_2(t) = [tr((S_{1y} + S_{2y})\rho(t = t_0 + dt)) - \text{mean}(tr((S_{1y} + S_{2y})\rho(t = t_0 + dt)))]$ until t = 0.1 ns from $t = t_0 = 0$ with a dt = 0.0002 ns step using the first and second equations in Eq(4).

(4) Calculate $S(t) = I_2(t) - iI_1(t)$.

(5) Carry out the Fourier transform of $S(t)$ and plot the result with respect to $\Delta\omega/2\pi$.

(6) Determine the $\Delta\omega/2\pi$ value in order to calculate the dependence of the microwave frequency as a function of $\omega_1/2\pi$, as shown in Figure S18.

(7) Then, calculate new $S(t)$ with respect to every $\omega_1/2\pi$ value using the $\Delta\omega/2\pi$ value determined in (6) and plot the Fourier transformed new $S(t)$ as a function of $\omega_1/2\pi$.

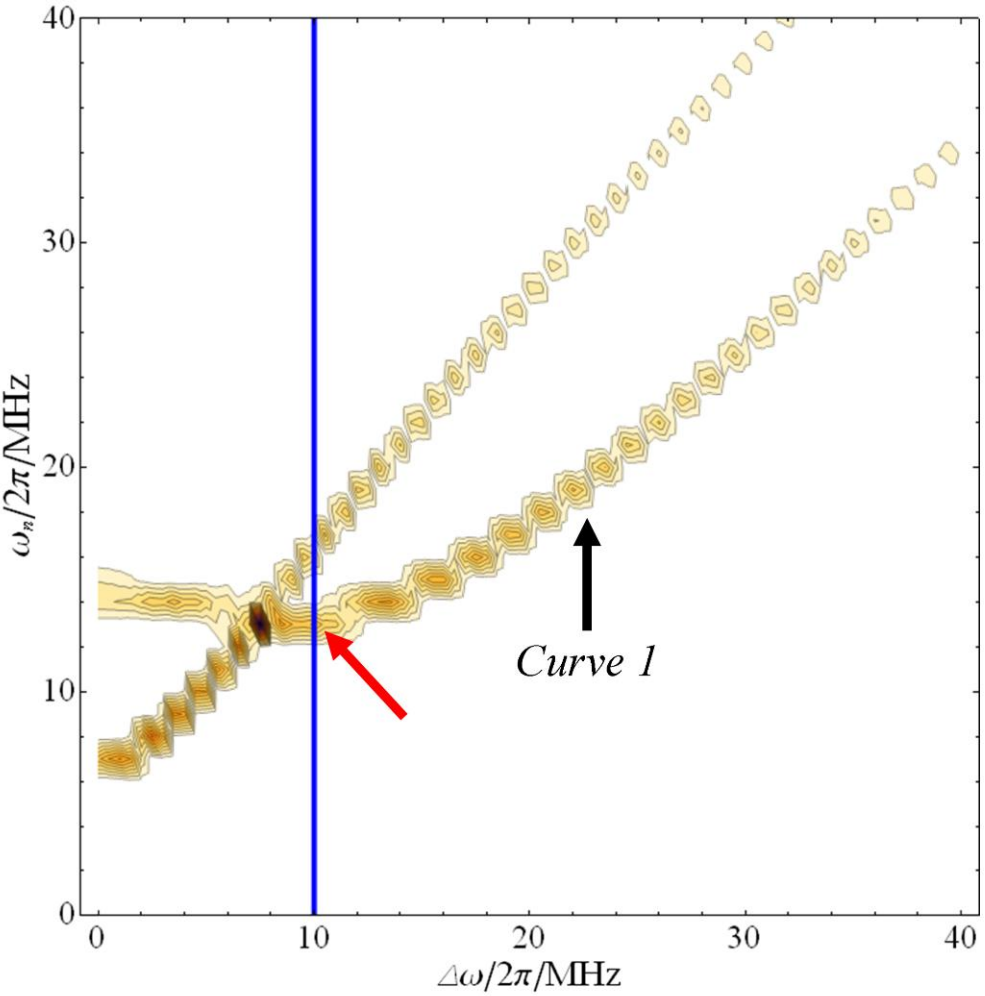

Figure S18. An example of the result of the numerical calculation (5) described above (D_{12} = –30 MHz, J_{12} = –10 MHz, Δg = 0, $\omega_1/2\pi$ = 10 MHz, at X-band). Curve 1 denotes the calculated result of the 2D-ESN signal in the FID-detected scheme. Then, the signal designated by the red arrow denotes the nutation frequency of the system. In order to calculate the ω_1-dependence of the nutation frequency, we determined the frequency difference $\Delta\omega/2\pi$, as shown with the blue vertical line (this process corresponds to the step (6) described above).

17. Analytical solutions for the ω_1-dependence of the nutation frequency with respect to the D_{xx}- or D_{yy}-direction for a non-zero E_{12} system.

For the system having a non-zero E_{12} value, the spin Hamiltonian (Eq (7) in the main text) is rewritten in the rotating frame. First of all, we perform the unitary transformation of the $\mathbf{D}_{12}$-tensor described in Eq (6) in order to describe the D_{xx}- and D_{yy}-principal axes in the coordinate system defined in the static magnetic field vector (changing the $\mathbf{D}_{12}$ into the $\mathbf{D}_{12,\,x\text{-}direct}$ or $\mathbf{D}_{12,\,y\text{-}direct}$ as schematically shown below).

$$\mathbf{D}_{12} = \begin{pmatrix} D_{12,xx} = -\frac{1}{3}D_{12} + E_{12} & & \\ & D_{12,yy} = -\frac{1}{3}D_{12} - E_{12} & \\ & & D_{12,zz} = \frac{2}{3}D_{12} \end{pmatrix}$$

$$\mathbf{D}_{12,\,x-direct} = \begin{pmatrix} D_{12,yy} & & \\ & D_{12,zz} & \\ & & D_{12,xx} \end{pmatrix}, \quad \mathbf{D}_{12,\,y-direct} = \begin{pmatrix} D_{12,zz} & & \\ & D_{12,xx} & \\ & & D_{12,yy} \end{pmatrix}$$

Secondly, we transform the unitary transformed spin Hamiltonian into the rotating frame with the resonance frequency $\nu_{MW} = \omega_0/2\pi + D'_{12}/4$. The transformed spin Hamiltonian is given as follows:

$$\begin{pmatrix} \frac{1}{12}\left(-4D_{12} \pm 3E_{12} + 3J_{12}\right) & \frac{(\omega_1/2\pi)}{2} & \frac{(\omega_1/2\pi)}{2} & \frac{\pm D_{12} - E_{12}}{4} e^{\frac{1}{2}i\{D_{12}+4(\omega_0/2\pi)\}t} \\ \frac{(\omega_1/2\pi)}{2} & \frac{1}{12}\left(D_{12} \mp 3E_{12} + 3J_{12}\right) & \frac{1}{12}\left(D_{12} \mp 3E_{12} + 6J_{12}\right) & \frac{(\omega_1/2\pi)}{2} \\ \frac{(\omega_1/2\pi)}{2} & \frac{1}{12}\left(D_{12} \mp 3E_{12} + 6J_{12}\right) & \frac{1}{12}\left(D_{12} \mp 3E_{12} + 3J_{12}\right) & \frac{(\omega_1/2\pi)}{2} \\ \frac{\pm D_{12} - E_{12}}{4} e^{-\frac{1}{2}i\{D_{12}+4(\omega_0/2\pi)\}t} & \frac{(\omega_1/2\pi)}{2} & \frac{(\omega_1/2\pi)}{2} & \frac{1}{12}\left(2D_{12} \pm 3E_{12} + 3J_{12}\right) \end{pmatrix}$$

where the $\mathbf{D}_{12,\,x\text{-}direct}$ or $\mathbf{D}_{12,\,y\text{-}direct}$ was transformed, upper or lower of the double signs designated, respectively. The elements (1,4) and (4,1) of the above matrix can be eliminated because these elements oscillate with the frequency four times larger than the Larmor frequency. Then, we derive the eigenvalues of the above matrix with the elements (1,4) and (4,1) set to zero, as follows:

$$\lambda_1' = -\frac{3}{4} J_{12}$$

$$\lambda_2' = \frac{1}{12}\left(3J_{12} + Y^{1/3} + Y^{*1/3} \right)$$

$$\lambda_3' = \frac{1}{24}\left\{ 6J_{12} - \left(1 - \sqrt{3}i\right) Y^{1/3} - \left(1 + \sqrt{3}i\right) Y^{*1/3} \right\}$$

$$\lambda_4' = \frac{1}{24}\left\{ 6J_{12} - \left(1 + \sqrt{3}i\right) Y^{1/3} - \left(1 - \sqrt{3}i\right) Y^{*1/3} \right\}$$

$$Y = -\left(D_{12} \mp 3E_{12}\right)\left\{ 8D_{12} \pm 6D_{12}E_{12} - 9\left(E_{12}^2 + 8\left(\omega_1/2\pi\right)^2\right) \right\}$$
$$+ 3\sqrt{3}\sqrt{9D_{12}^2E_{12}^2\left(2D_{12} \mp 3E_{12}\right)^2 + 16D_{12}^2\left(8D_{12}^2 \mp 30D_{12}E_{12} + 45E_{12}^2\right)\left(\omega_1/2\pi\right)^2}$$
$$\overline{+ 64\left(13D_{12}^2 \mp 6D_{12}E_{12} + 9E_{12}^2\right)\left(\omega_1/2\pi\right)^4 + 4096\left(\omega_1/2\pi\right)^6}\, i$$

where the meaning of the double signs is kept. Y^* denotes the complex conjugate of Y. All the eigenvalues are real.

From these equations, the eigenvalues expressed in Eq(8) of the main text are derived by setting $E_{12} = 0$ and $D_{12} = -2D'_{12}$.

18. Canonical peak/off-principal axis extra line assignments based on the angular dependence of the X-/Q-band simulated CW ESR spectra of biradical 1 in the principal coordinate system.

The canonical peak and off-principal axis extra line assignments for the observed spectra shown in Fig. 2 of the main text are based on the angular dependence of the simulated spectra, as depicted in Figs. S19-21 for the Q-band microwave frequency and in Figs. S22-24 for the X-band frequency, respectively. The definition of the canonical orientations is given in Fig. 3 of the main text. The angular dependence in terms of the principal axis system is calculated with the experimentally determined spin Hamiltonian parameters (the magnetic tensors). Particularly, we note that the E_{12} value is vanishing. In the analysis of the assignments, the off-principal axis extra lines have been identified in both the X- and Q-band spectra. The angle regions at which the extra lines appear are denoted by thick orange arrows.

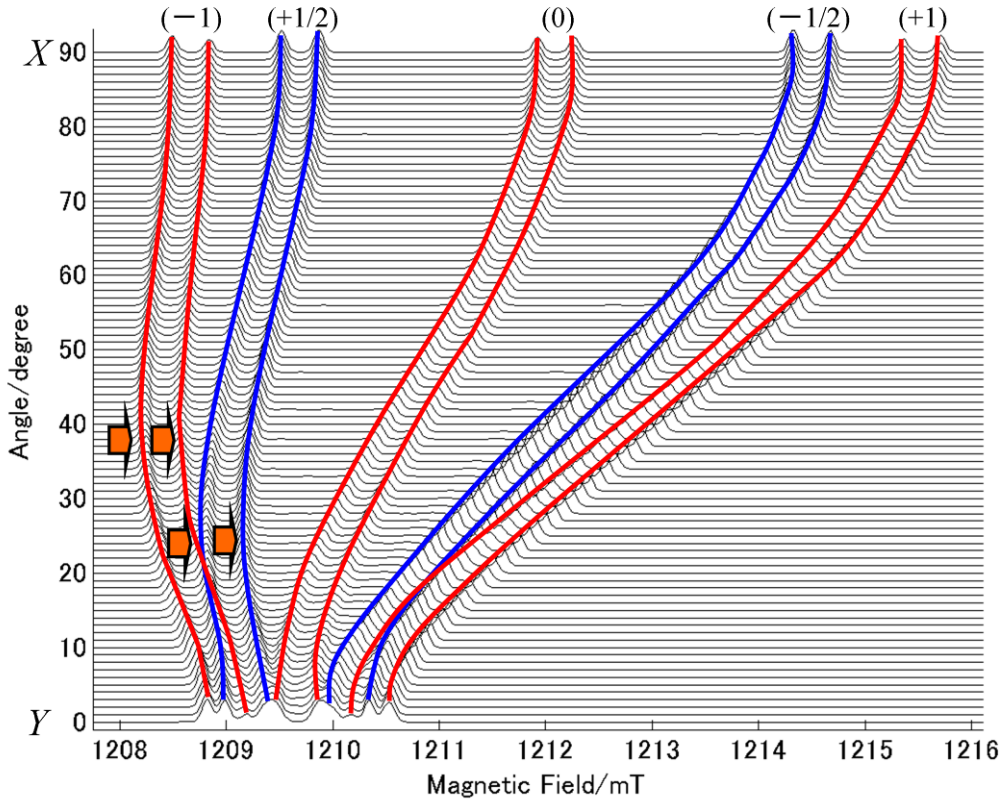

Figure S19. Angular dependence of the Q-band CW ESR spectra (simulated) in the *XY* plane, which is defined in Fig. 3 in the main text. The red and blue lines denote the absorption peaks due to the ^{14}N and ^{15}N hyperfine transitions, respectively. The lines trace the peak tops of the absorptions. The numbers in the parentheses denote the nuclear spin magnetic quantum numbers of the nitrogen nuclei. The angle regions at which the extra lines appear are denoted by thick orange arrows.

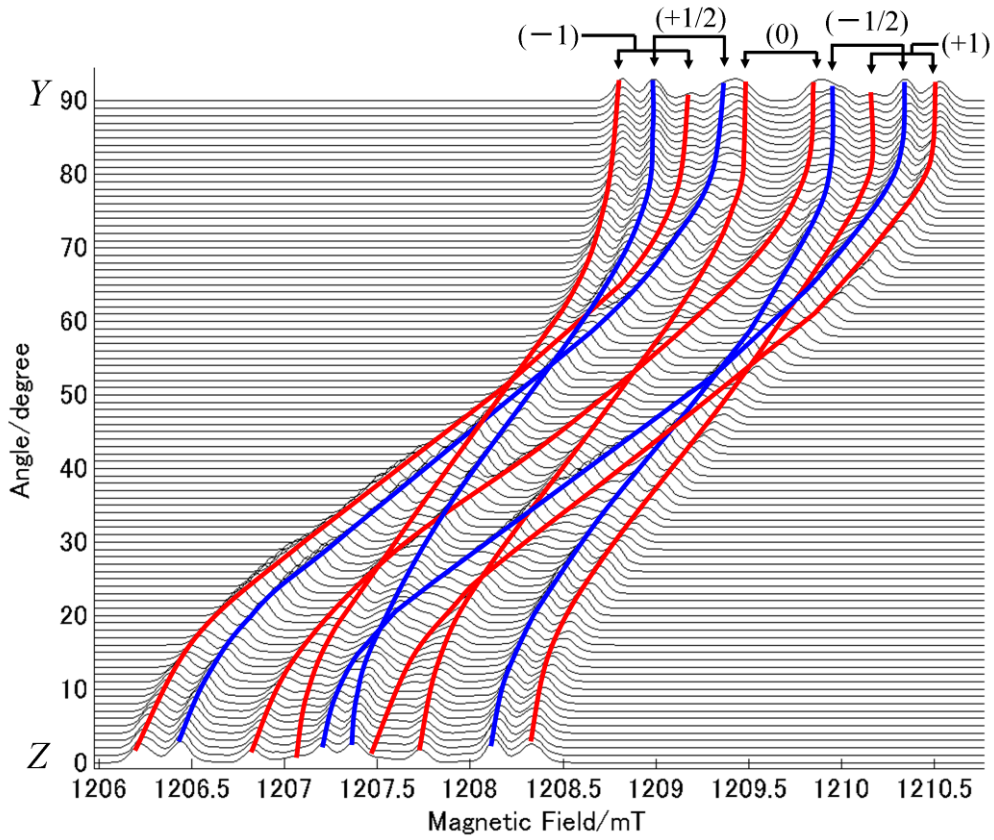

Figure S20. Angular dependence of the Q-band CW ESR spectra (simulated) in the *YZ* plane, which is defined in Fig. 3 in the main text. The red and blue lines show the signals due to the ^{14}N and ^{15}N hyperfine splitting, respectively. The red and blue lines denote the absorption peaks due to the ^{14}N and ^{15}N hyperfine transitions, respectively. The lines trace the peak tops of the absorptions. The numbers in the parentheses denote the nuclear spin magnetic quantum numbers of the nitrogen nuclei.

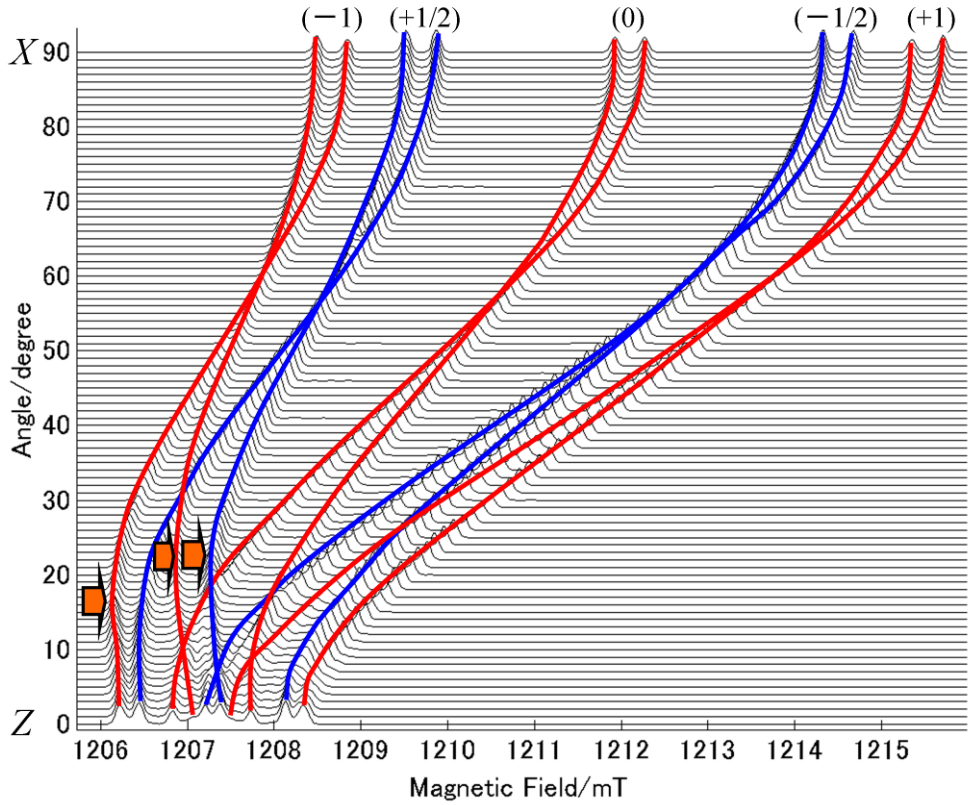

Figure S21. Angular dependence of the Q-band CW ESR spectra (simulated) in the *ZX* plane, which is defined in Fig. 3 in the main text. The red and blue lines denote the absorption peaks due to the ^{14}N and ^{15}N hyperfine transitions, respectively. The lines trace the peak tops of the absorptions. The numbers in the parentheses denote the nuclear spin magnetic quantum numbers of the nitrogen nuclei. The angle regions at which the extra lines appear are denoted by thick orange arrows.

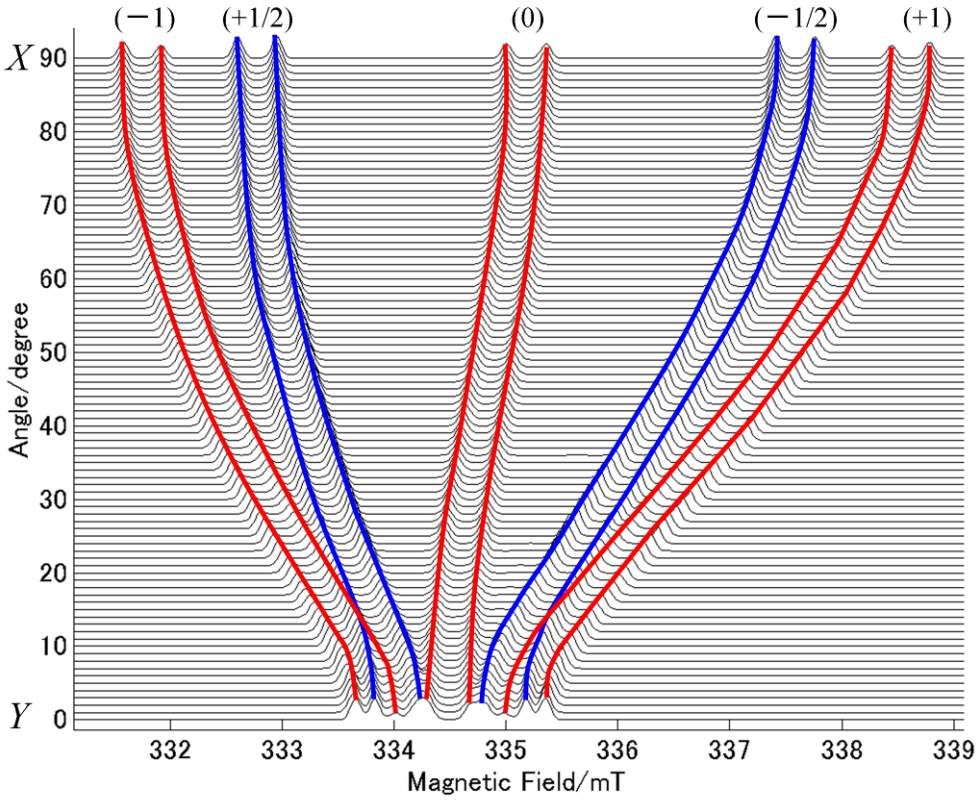

Figure S22. Angular dependence of the X-band CW ESR spectra (simulated) in the *XY* plane, which is defined in Fig. 3 in the main text. The red and blue lines denote the absorption peaks due to the ^{14}N and ^{15}N hyperfine transitions, respectively. The lines trace the peak tops of the absorptions. The numbers in the parentheses denote the nuclear spin magnetic quantum numbers of the nitrogen nuclei.

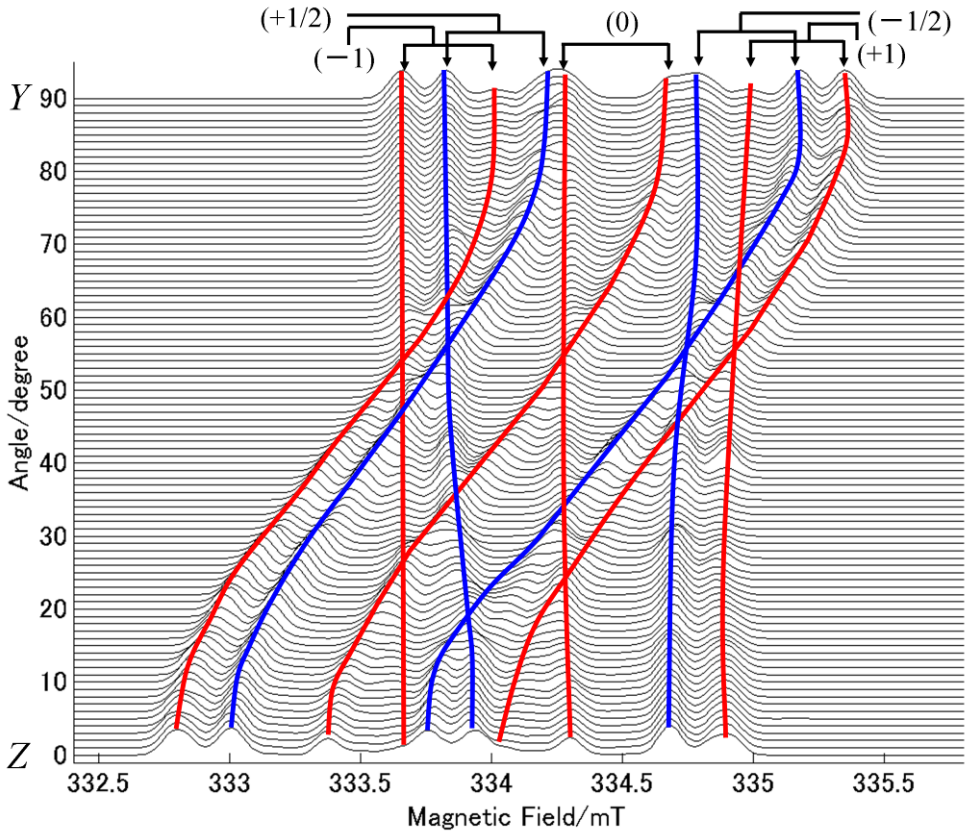

Figure S23. Angular dependence of the X-band CW ESR spectra (simulated) in the *YZ* plane, which is defined in Fig. 3 in the main text. The red and blue lines denote the absorption peaks due to the ^{14}N and ^{15}N hyperfine transitions, respectively. The lines trace the peak tops of the absorptions. The numbers in the parentheses denote the nuclear spin magnetic quantum numbers of the nitrogen nuclei.

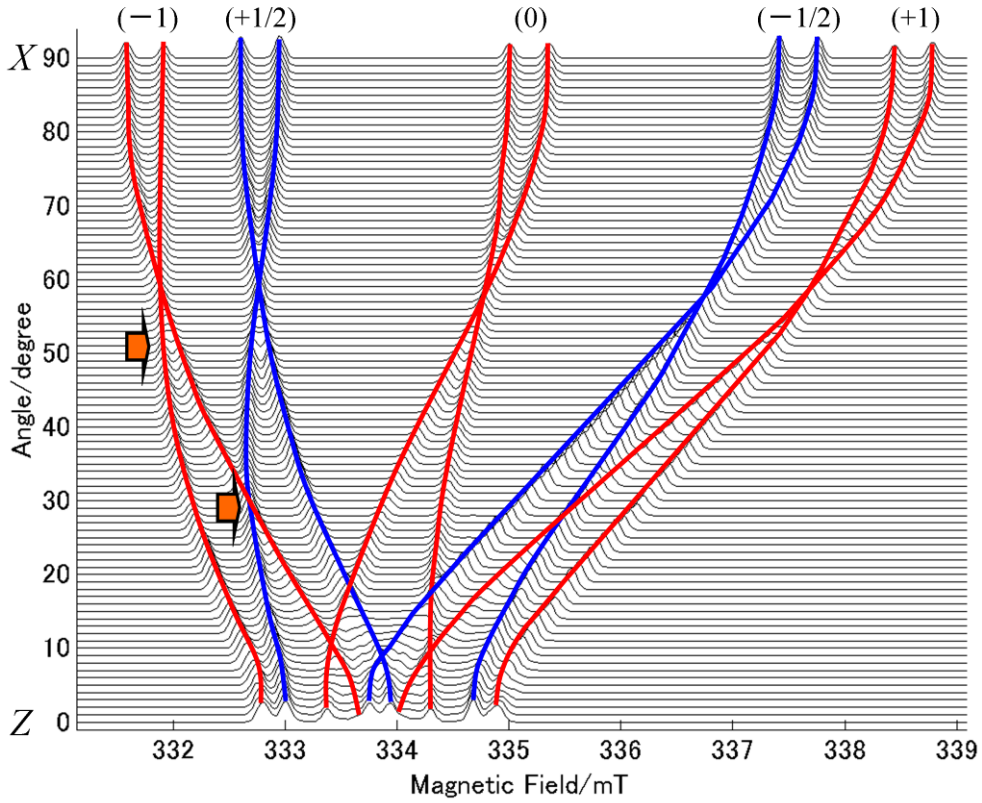

Figure S24. Angular dependence of the X-band CW ESR spectra (simulated) in the *ZX* plane, which is defined in Fig. 3 in the main text. The red and blue lines denote the absorption peaks due to the ^{14}N and ^{15}N hyperfine transitions, respectively. The lines trace the peak tops of the absorptions. The numbers in the parentheses denote the nuclear spin magnetic quantum numbers of the nitrogen nuclei. The angle regions at which the extra lines appear are denoted by thick orange arrows.

19. The effect of hyperfine interactions on the nutation behaviour for the *Y*- and *X*-canonical orientations in biradical 1

Figures S25, S26, S27, S28, S29 and S30 show the contour plots of the nutation frequencies numerically calculated with all the nitrogen nuclear (one ^{14}N nucleus and one ^{15}N nucleus) hyperfine interactions taken into account. Figs. S25, S26 and S27 are for the *Y*-canonical orientation, and Figs. S28, S29 and S30 are for the *X*-canonical orientation at the same magnetic field that the nutation experiments at X-band were carried out. The principal values of the hyperfine interactions are small for the *Y*-orientation, while those are the largest for the *X*-orientation. For the *Y*-orientation, the behaviour of the calculated nutation frequencies with the nitrogen hyperfine interactions taken into account is consistent with the ω_1-dependence obtained in terms of the analytical expressions derived in this work, as shown in Figs. S25, S26 and S27. On the other hand, for the *X*-direction in which the largest principal values of the hyperfine tensors appear, the nutation frequencies calculated with the hyperfine interactions taken into account are significantly lower than those obtained without the hyperfine interactions, as shown in Figs. S28, S29 and S30. Thus, we have quantitatively estimated the error for the experimental D_{12} value determined by the present X-band ESN spectroscopy for the canonical orientations of biradical **1** to be 2-3 MHz.

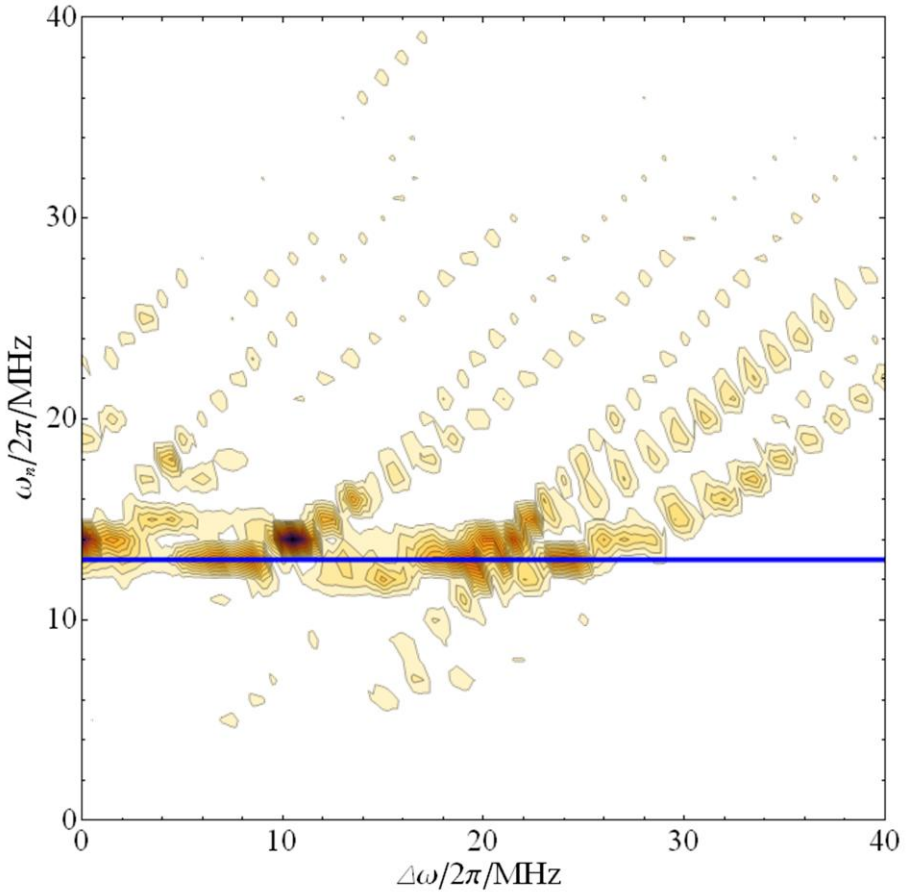

Figure S25. Contour plot of the nutation frequency, ω_n, numerically calculated with the hyperfine interactions (one ^{14}N nucleus and one ^{15}N nucleus) taken into account (step (5) in Section 16) for the *Y*-canonical orientation of biradical **1** ($\omega_1/2\pi$ = 10 MHz). See the main text for the resonance field at X-band. The blue horizontal line denotes the nutation frequency calculated without the hyperfine interactions due to the nitrogen nuclei (^{14}N and ^{15}N) by using the analytical expressions derived from the only four electronic spin states for biradical **1**.

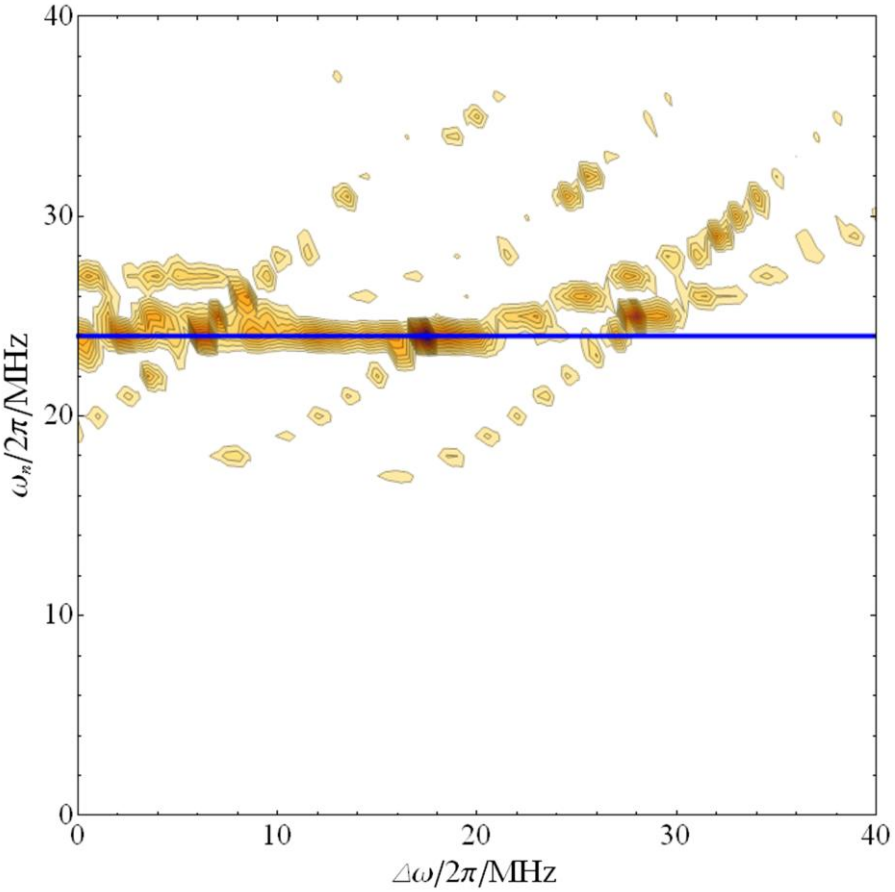

Figure S26. Contour plot of the nutation frequency, ω_n, numerically calculated with the nitrogen hyperfine interactions (one ^{14}N nucleus and one ^{15}N nucleus) taken into account (step (5) in Section 16) for the *Y*-canonical orientation of biradical **1** ($\omega_1/2\pi$ = 20 MHz). See the main text for the resonance field at X-band. The blue horizontal line denotes the nutation frequency calculated without the hyperfine interactions due to the nitrogen nuclei (^{14}N and ^{15}N) by using the analytical expressions derived from the only four electronic spin states for biradical **1**.

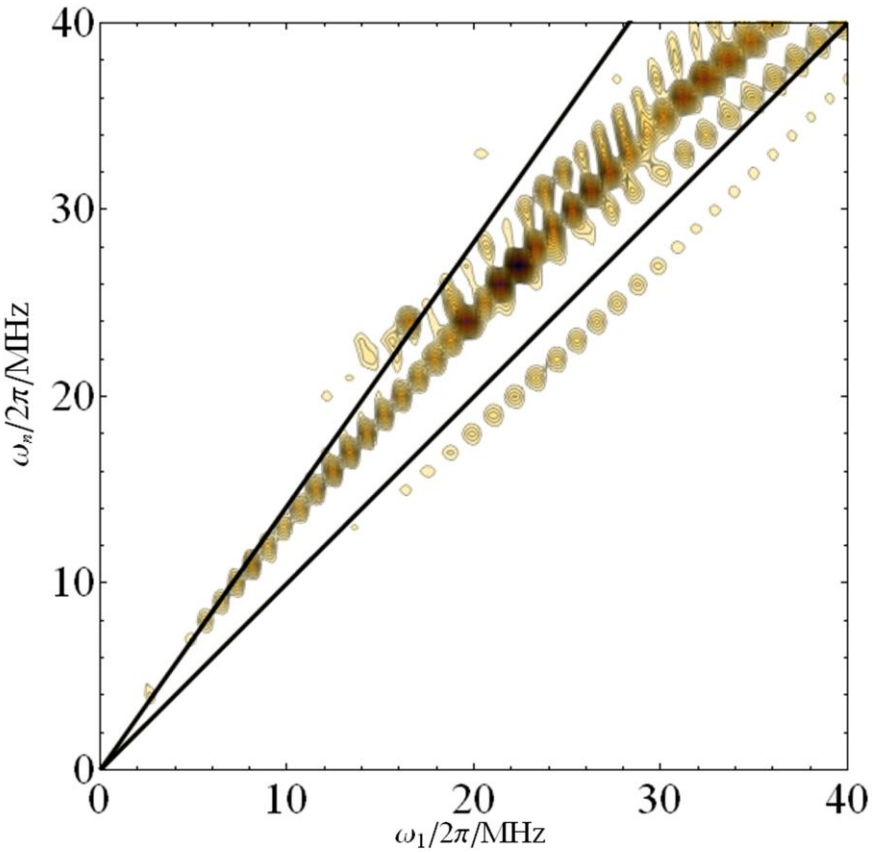

Figure S27. ω_1-Dependence of the nutation frequency for the *Y*-canonical orientation calculated with the nitrogen hyperfine interactions (one ^{14}N nucleus and one ^{15}N nucleus) taken into account. The upper black line denotes the behaviour of $\omega_n = \sqrt{2}\ \omega_1$ for extreme case, i.e. an isolated triplet state. The lower line indicates the nutation behaviour of isolated spin-doublets, i.e. $\omega_n = \omega_1$. The dependence agrees with that of the analytically calculated without the hyperfine interaction.

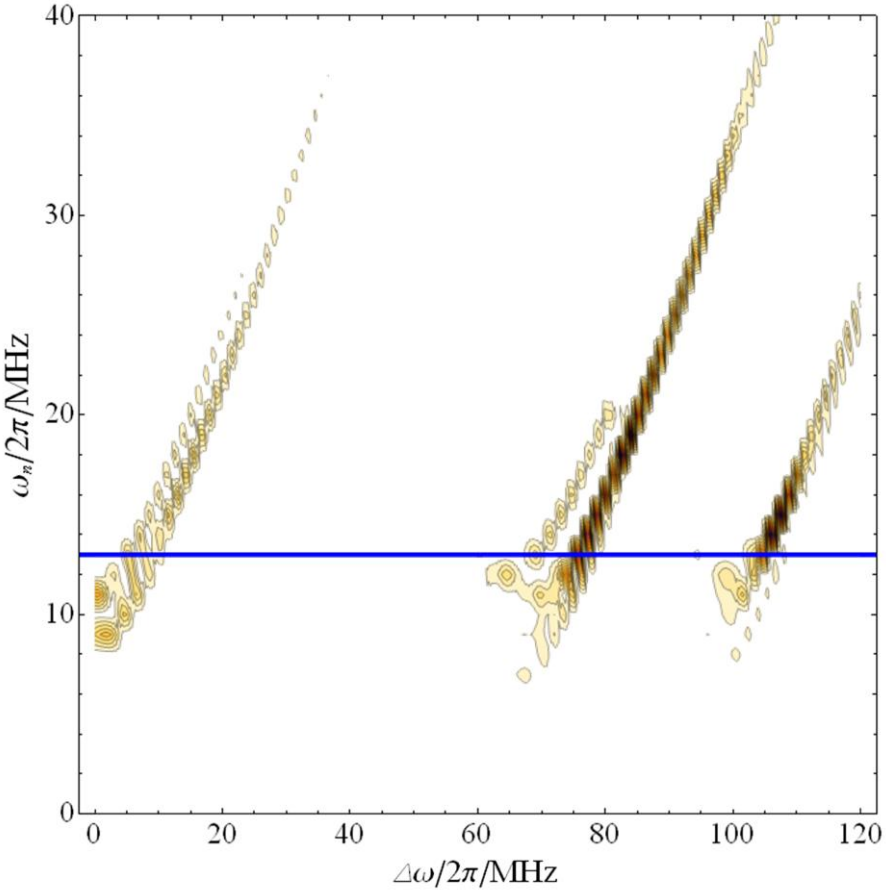

Figure S28. Contour plot of the nutation frequency, ω_n, numerically calculated with the hyperfine interactions (one ^{14}N nucleus and one ^{15}N nucleus) taken into account (step (5) in Section 16) for the *X*-canonical orientation of biradical **1** ($\omega_1/2\pi$ = 10 MHz). See the main text for the resonance field at X-band. The blue horizontal line denotes the nutation frequency calculated without the hyperfine interactions due to the nitrogen nuclei (^{14}N and ^{15}N) by using the analytical expressions derived from the only four electronic spin states for biradical **1**.

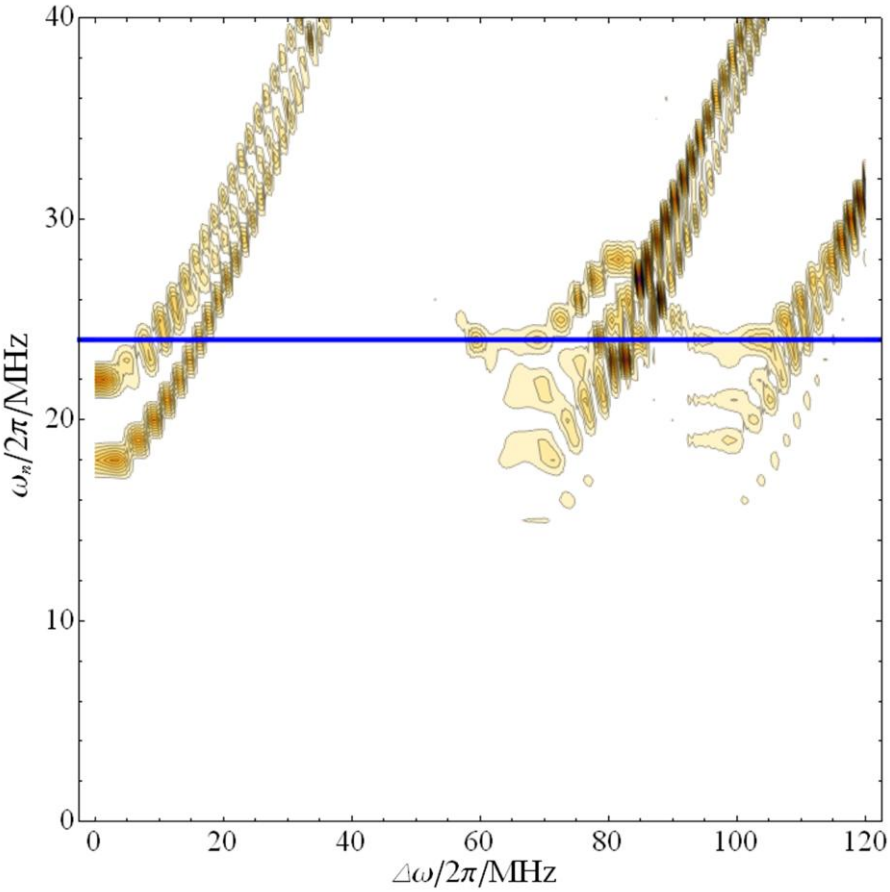

Figure S29. Contour plot of the nutation frequency, ω_n, numerically calculated with the hyperfine interactions (one ^{14}N nucleus and one ^{15}N nucleus) taken into account (step (5) in Section 16) for the *X*-canonical orientation of biradical **1** ($\omega_1/2\pi$ = 20 MHz). See the main text for the resonance field at X-band. The blue horizontal line denotes the nutation frequency calculated without the hyperfine interactions due to the nitrogen nuclei (^{14}N and ^{15}N) by using the analytical expressions derived from the only four electronic spin states for biradical **1**.

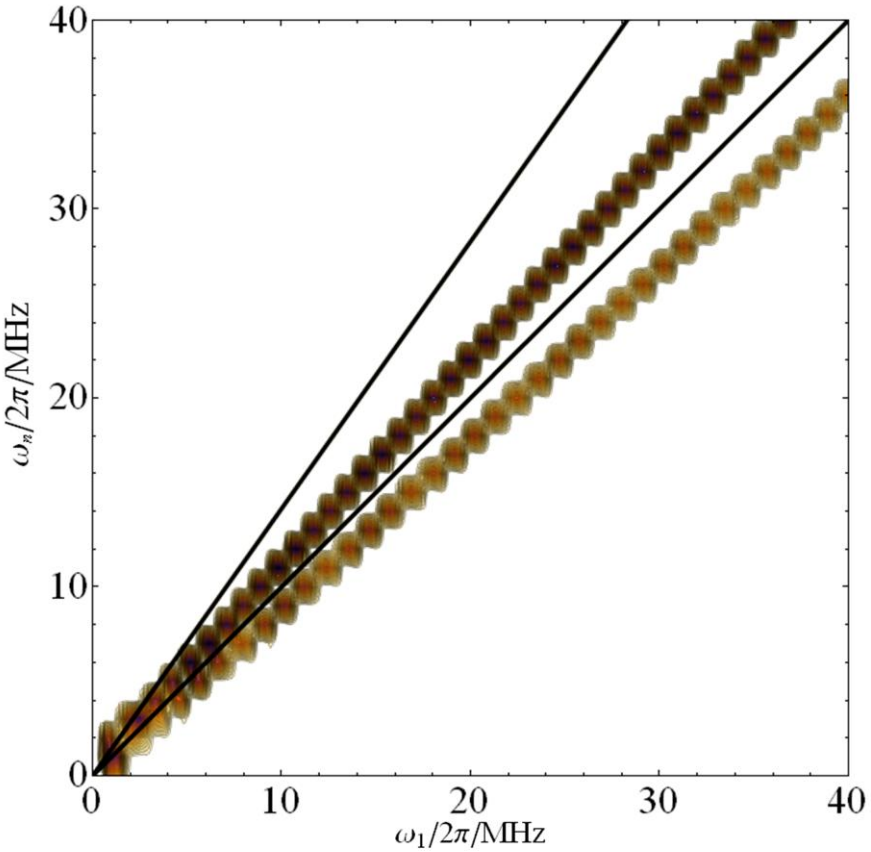

Figure S30. ω_1-Dependence of the on-resonance nutation frequency for the *X*-canonical orientation calculated with the nitrogen hyperfine interactions (one ^{14}N nucleus and one ^{15}N nucleus) taken into account. The upper black line denotes the behaviour of $\omega_n = \sqrt{2}\ \omega_1$ for extreme case, i.e. an isolated triplet state. The lower line indicates the nutation behaviour of isolated spin-doublets, i.e. $\omega_n = \omega_1$. The calculated points between the two black lines, which have the larger intensities, exactly correspond to the single-dotted dashed line of Fig. 5 in the main text.

References:

[S1] S. Stoll, A. Schweiger, *J. Magn. Reson.*, 2006, **178**, 42–55.
[S2] H. Kameya, H. Nakamura, M. Ukai, Y. Shimoyama, *Spectrocimica Acta Part A*, 2008, **69**, 1367–1371.
[S3] K. N. Hu, C. Song, H. H. Yu, T. M. Swager, R. G. Griffin, *J. Chem. Phys.*, 2008, **128**, 052302/1–052302/17.
[S4] S. Stoll, G. Jeschke, M. Willer, A. Schweiger, *J. Magn. Reson.*, 1998, **130**, 86–96.
[S5] L. V. Kulik, S. A. Dzuba, I. A. Grigoryev, Yu. D.Tsvetkov, *Chem. Phys. Lett.*, 2001, **343**, 315–324.
[S6] S. Sinnecker, F. Neese, *J. Phys. Chem. A*, 2006, **110**, 12267–12275.
[S7] K. Sugisaki, K. Toyota, K. Sato, D. Shiomi, M. Kitagawa, T. Takui, *ChemPhysChem*, 2010, **11**, 3146–3151.
[S8] M. Shoji, K. Koizumi, T. Hamamoto, T. Taniguchi, R. Takeda, Y. Kitagawa, T. Kawakami, M. Okumura, S. Yamanaka, K. Yamaguchi, *Polyhedron*, 2005, **24**, 2708–2715.
[S9] T. T. Petrenko, T. L. Petrenko, V. Y. Bratus, *J. Phys. Condens. Matter.*, 2002, **14**, 12433–12440.
[S10] R. McWeeny, Y. Mizuno, *Proc. R. Soc. London, Ser. A*, 1961, **259**, 554-577.
[S11] K. Yamaguchi, *Chem. Phys. Lett.*, 1975, **33**, 330–335.
[S12] M. J. Frisch, G. W. Trucks, H. B. Schlegel, G. E. Scuseria, M. A. Robb, J. R. Cheeseman, J. A. Montgomery, Jr., T. Vreven, K. N. Kudin, J. C. Burant, et al., *Gaussian 03*, revision B.05; Gaussian, Inc.; Pittsburgh, PA, 2003.
[S13] A. Weber, O. Schiemann, B. Bode, T. F. Prisner, *J. Magn. Reson.*, 2002, **157**, 277-285.
[S14] G. Jeschke, *Macromol. Rapid Commun.*, 2002, **23**, 227-246.
[S15] A. D. Milov, A. G. Maryasov, Yu. D. Tsvetkov, *Appl. Magn. Reson.*, 1998, **15**, 107-143.